Diamond & Related Materials 163 (2026) 113399

Contents lists available at ScienceDirect

Diamond & Related Materials

journal homepage: www.elsevier.com/locate/diamond

Enhanced hydrogen storage in lithium-doped defective fullerenes: Experimental optimization, adsorption mechanisms, and kinetic–isotherm modeling

Yasemin Turhan [a], Betül Duman [a], Mehmet Doğan [a,*], Ersin Yanmaz [b], Zeynep Bicil [a], Berna Koçer Kızılduman [a]

[a] Balikesir University, Faculty of Science and Literature, Department of Chemistry, 10145, Çağış, Balıkesir, Turkey
[b] Balikesir University, Altınoluk Vocational School, Department of Chemical and Chemical Processing Technologies, 10870, Altınoluk, Balıkesir, Turkey

ARTICLE INFO

Keywords:
Fullerene
Li-doping
Hydrothermal method
Hydrogen storage
Isotherm
Kinetics

ABSTRACT

This study investigates the enhancement of hydrogen storage capacity in fullerene (C60) through lithium doping and defect formation. Defective fullerenes (D—C60) were synthesized via high-energy ball milling, and Li-doped variants were prepared using hydrothermal methods. FTIR revealed the disappearance of C60's characteristic bands and the emergence of new bands in doped and defective samples. Thermal analysis showed reduced stability and altered degradation mechanisms due to defect formation and lithium incorporation. SEM indicated significant morphological changes, with increased agglomeration in Li-doped particles. Particle size variations and symmetry loss were also observed post-milling.

Hydrogen storage performance depended on lithium concentration, temperature, and doping time. Among tested samples, the sample doped with 0.1 M $LiNO_3$ at 200 °C for 12 h (Li-D-C60–01 M-200C-12 h) showed the highest hydrogen uptake, attributed to its large surface area and micropore volume under high-pressure adsorption conditions and cryogenic temperatures, where excess adsorption behavior was observed.

Isotherm models fitted well with Freundlich and Langmuir equations, while kinetic data followed the pseudo-second-order model, indicating intra-particle diffusion as the rate-limiting step. EIS analysis demonstrated improved conductivity and reduced impedance in Li-doped samples due to enhanced diffusion-based charge transport. Pearson correlation analysis revealed strong positive relationships between hydrogen storage capacity and both BET surface area ($r = 0.9033$) and micropore volume ($r = 0.8867$), with the dominant influence arising from BET surface area; this indicates that Li doping affects performance primarily through modifications in pore accessibility and surface electronic structure.

Moreover, Li centers act as controllable hydrogen release valves, enabling safer and more reversible hydrogen desorption compared to pristine fullerene systems. These results demonstrate the promising potential of Li-doped defective fullerenes in hydrogen storage applications.

1. Introduction

Hydrogen is widely recognized as a clean and sustainable energy carrier with the potential to reduce greenhouse gas emissions by replacing fossil fuels [1]. Its high gravimetric energy density and environmentally benign combustion products make it attractive for energy, transportation, and industrial applications. However, the safe and efficient storage of hydrogen in large quantities remains a major technological challenge [2]. Conventional storage methods, including compressed gas, cryogenic liquid hydrogen, and metal hydrides, suffer from safety concerns, high costs, and kinetic limitations [3]. Therefore, physical hydrogen storage in porous solid adsorbents has emerged as a promising alternative. Various porous materials, such as zeolites [4], metal–organic frameworks (MOFs) [5], covalent organic frameworks (COFs) [6], boron nitride derivatives, activated carbons [7], carbon spheres [8], graphene [9], and carbon nanotubes [10], have been

* Corresponding author.
E-mail addresses: yozdemir@balikesir.edu.tr (Y. Turhan), betul.duman22@gmail.com (B. Duman), mdogan@balikesir.edu.tr (M. Doğan), ersinyanmaz@balikesir.edu.tr (E. Yanmaz), zeynepbicil@balikesir.edu.tr (Z. Bicil), bernakocer@balikesir.edu.tr (B.K. Kızılduman).

https://doi.org/10.1016/j.diamond.2026.113399
Received 1 September 2025; Received in revised form 23 January 2026; Accepted 1 February 2026
Available online 3 February 2026

extensively investigated for hydrogen storage. Nevertheless, their storage capacities generally remain below target values, and their gravimetric capacities and desorption kinetics are still insufficient for practical implementation. Thus, the development of advanced carbon-based adsorbents with enhanced hydrogen storage performance is still required.

Fullerenes represent a unique class of carbon allotropes with well-defined molecular structures and tunable electronic properties. Theoretical studies have predicted that fullerenes may exhibit high hydrogen storage capacities; for instance, modeling results suggested that up to 58 hydrogen atoms (≈8 wt%) can be incorporated into a C60 cage [11]. Grand canonical Monte Carlo simulations further indicated that hydrogen incorporation barriers can be reduced through hydrogenation, potentially enabling storage capacities up to 7.71 wt% under ambient conditions [12]. In addition, hydrogenation mechanisms in alkali-metal-intercalated fullerites, such as Li_6C_{60}, have been investigated, and μSR measurements suggested higher hydrogen storage capacities than previously reported [13].

Despite these promising theoretical predictions, experimental studies on fullerene-based hydrogen storage materials remain limited. In one of the few experimental studies, lithium- and sodium-doped fullerenes exhibited hydrogen storage capacities of 5.0 wt% and 4.0 wt%, respectively [14]. In another study, defective fullerenes produced by high-energy ball milling showed enhanced textural properties, and the defective fullerene ground at 500 rpm for 1 h (D-C60–1 h-500 rpm) achieved a hydrogen storage capacity of 2.17 wt%, which increased with defect density [15]. However, no experimental study has systematically evaluated the effect of lithium doping on the hydrogen storage performance of defective fullerenes, nor investigated the corresponding adsorption isotherms, kinetics, and adsorption mechanisms.

Although several theoretical studies have predicted high hydrogen storage potential for fullerene-based structures, experimental validation remains scarce, particularly for lithium-doped defective fullerenes. Moreover, no comprehensive study has optimized Li-doping parameters such as concentration, temperature, and reaction time or correlated the resulting structural changes with adsorption isotherms, kinetics, electrochemical impedance behavior, and pressure-dependent hydrogen uptake at both room and cryogenic temperatures. This lack of integrated experimental evidence highlights a critical research gap.

Recently, two-dimensional fullerene networks have been reported to exhibit remarkable hydrogen storage capacities due to combined chemisorption and physisorption mechanisms [16]. These findings further demonstrate the potential of fullerene-based architectures for hydrogen storage and motivate the present experimental investigation of Li-doped defective fullerene systems. In this context, the novelty of the present work lies in the development of an experimentally accessible defect–dopant co-engineered fullerene system for hydrogen storage, where structural defect formation and Li doping are synergistically combined to tailor pore accessibility, surface electronic structure, and adsorption energetics. Unlike recently reported two-dimensional fullerene lattices that exhibit extraordinary theoretical hydrogen storage capacities but remain synthetically challenging, the present Li-doped defective fullerene architecture provides a structurally simpler and scalable platform with controllable hydrogen adsorption–desorption behavior. Importantly, Li atoms act as hydrogen release valves, enabling safer and more reversible hydrogen storage compared to pristine fullerene systems. Furthermore, this study establishes a quantitative correlation between textural properties, adsorption thermodynamics, kinetics, diffusion mechanisms, and electrochemical impedance behavior, offering mechanistic insights and a realistic pathway toward practical fullerene-based hydrogen storage materials. Accordingly, the aims of this study are: (i) to synthesize defective fullerenes via high-energy ball milling, (ii) to systematically tune their textural properties through Li doping under different concentrations, temperatures, and reaction times using a hydrothermal approach, (iii) to comprehensively characterize the structural, morphological, and surface chemical properties of the materials, (iv) to evaluate the pressure-dependent hydrogen storage capacities at room and cryogenic temperatures, and (v) to elucidate adsorption kinetics and diffusion mechanisms. To the best of our knowledge, this study represents one of the most comprehensive experimental investigations of hydrogen storage in Li-doped defective fullerenes, providing mechanistic insights supported by combined structural, textural, and electrochemical analyses.

2. Materials and methods

2.1. Materials

Fullerene (C60, 99% purity) was purchased from Nanografi (Turkey), $LiNO_3$ was purchased from Leverton Clarke Ltd. (UK), and all other chemicals were of analytical grade and used without further purification.

2.2. Methods

2.2.1. Production of defective fullerene

Defective fullerenes were produced by ball milling pristine fullerene in a high-energy tungsten carbide ball mill at 500 rpm for 1 h, as reported previously [15].

2.2.2. Lithium doping of defective fullerene

Lithium doping of defective fullerenes was carried out using a hydrothermal method under different concentrations, temperatures, and reaction times.

For this purpose, 0.5 g of defective fullerene was dispersed in 15 mL $LiNO_3$ solutions with concentrations of 0.1, 0.01, and 0.001 M in a 20 mL Teflon-lined stainless-steel autoclave. The suspension was hydrothermally treated at 200 °C for 6 h. After the reaction, the reactor was naturally cooled to room temperature for 6 h. The resulting suspension was filtered and sequentially washed with deionized water and ethanol. The obtained solid was dried at 105 °C for 24 h.

Based on BET surface area and pore volume results, the Li-D-C60–01 M-200C-6 h sample was selected for temperature optimization. To investigate the effect of temperature, experiments were conducted at 160, 200, and 240 °C for 6 h at 0.1 M $LiNO_3$ concentration. The Li-D-C60–01 M-200C-6 h sample was identified as the optimized material. Subsequently, the effect of reaction time was examined at 200 °C for 2, 6, and 12 h at 0.1 M $LiNO_3$ concentration. Li-D-C60–01 M-200C-12 h was determined as the sample with the highest BET surface area and pore volume values [17].

2.2.3. Electrochemical impedance spectroscopy (EIS) measurements

Electrochemical impedance spectroscopy (EIS) measurements were performed at room temperature using a conventional three-electrode system. A platinum plate was used as the counter electrode, Ag/AgCl (saturated KCl) as the reference electrode, and a glassy carbon electrode as the working electrode. The samples were dispersed in sodium dodecyl sulfate (SDS) solution and drop-cast onto the working electrode surface, followed by drying under ambient conditions. Measurements were performed using a Metrohm VIONIC Autolab electrochemical workstation controlled by INTELLO software (v1.6). An AC voltage amplitude of 10 mV was applied over a frequency range of 1 Hz to 10 kHz. The impedance data were recorded and analyzed using the same software [18].

2.2.4. Hydrogen storage measurements

Hydrogen storage capacities were measured using a Hiden IMI PSI high-pressure volumetric gas storage analyzer. Prior to analysis, the samples were degassed at 105 °C for 24 h. Hydrogen storage capacities were determined at room and cryogenic temperatures under various pressures [18,19].

2.2.5. Characterization

Pristine fullerene, defective fullerene, and Li-doped defective fullerene samples were comprehensively characterized to elucidate their structural, textural, morphological, and surface chemical properties. The Brunauer–Emmett–Teller (BET) surface area and pore structure were determined by N_2 adsorption–desorption measurements using a Quantachrome Nova 2200e surface area analyzer after degassing the samples at 105 °C for 24 h. Surface functional groups and chemical modifications induced by defect formation and lithium doping were analyzed by Fourier transform infrared spectroscopy (FTIR) using a PerkinElmer Spectrum 100 spectrometer. Crystallographic structure and phase changes were investigated by X-ray diffraction (XRD) using a PANalytical Empyrean diffractometer equipped with CuKα radiation (λ = 1.5418 Å). Thermal stability and decomposition behavior were examined using differential thermal analysis/thermogravimetric analysis (DTA/TG) on a PerkinElmer Diamond DTA/TG system under a nitrogen atmosphere. Morphological characteristics and elemental composition were analyzed by scanning electron microscopy coupled with energy-dispersive X-ray spectroscopy (SEM/EDX) using a Zeiss EVO LS 10 microscope equipped with a Bruker EDX detector. Transmission electron microscopy (TEM) was performed on a Hitachi HT7800 instrument to visualize internal microstructural features and defect-induced structural changes. Surface chemical states and bonding environments were investigated by X-ray photoelectron spectroscopy (XPS) using a SPECS Flex XPS spectrometer with monochromatized AlKα radiation. Additionally, atomic force microscopy (AFM) measurements were conducted using a Nanosurf Easyscan 2 AFM in tapping mode to evaluate surface topography and nanoscale roughness. These complementary characterization techniques provided a comprehensive understanding of the effects of defect engineering and lithium doping on the structural and surface properties of fullerene-based materials [15].

3. Results and discussion

3.1. Characterization

3.1.1. FTIR analysis

Fig. 1 shows the FTIR spectra of fullerene, defective fullerene, and Li-doped defective fullerene samples. Pristine fullerene exhibits four characteristic bands at 1427, 1182, 576, and 527 cm^{-1}, which are typical vibrational modes of the C_{60} cage structure [20]. After 1 h of ball milling, these characteristic bands disappeared, and a new sharp band emerged at 1383 cm^{-1}, indicating the transformation of the pristine C_{60} structure into a defective form. This band was attributed to the C—C vibration mode associated with the coexistence of sp^2 and sp^3 hybridization and may also correspond to C—H bending vibrations [15].

Significant structural changes were observed in the range of ~3300 cm^{-1} after lithium doping of defective fullerenes, which were attributed to the presence of hydroxyl groups and possible carboxyl group formation induced by the hydrothermal process [8]. Previous studies reported that lithium doping can expand C—C bond lengths and alter the geometric configuration of the fullerene cage, thereby affecting its stability and physicochemical properties [21].

A comparison of the FTIR spectra of fullerene, defective fullerene, and Li-doped defective fullerene reveals an increasing intensity of hydroxyl peaks in the range of 3330–3340 cm^{-1} with hydrothermal treatment and lithium incorporation. Furthermore, three vibration bands assigned to Li—O stretching modes were detected in the range of 650–690 cm^{-1} for the Li-doped samples, providing direct evidence of successful lithium doping. Fig. 1 also illustrates the influence of concentration, temperature, and reaction time on the doping process, where progressively intensified hydroxyl and Li—O bands confirm the increasing degree of surface functionalization and Li incorporation.

The bands observed at 2923 and 2852 cm^{-1} in fullerene, defective fullerene, and Li-doped defective fullerene samples are attributed to C—H stretching vibrations of sp^3-hybridized carbon atoms. Additionally, vibrational features in the range of 1610–1630 cm^{-1} were assigned to residual $LiNO_3$-related species in the Li-doped samples.

3.1.2. XRD analysis

Fig. 2 shows the XRD patterns of fullerene, defective fullerene, and Li-doped defective fullerene samples. The patterns were evaluated separately to clarify the effects of Li concentration, temperature, and reaction time on the crystalline structure. In our previous study, which represents the first experimental report on mechanically induced defective fullerene formation, the characteristic 2θ reflections of pristine fullerene were identified at 10.79°, 17.70°, 20.77°, 21.70°, 27.39°, 28.12°, 30.91°, and 32.80° [15]. These diffraction peaks correspond to the (111), (220), (311), (222), (331), (420), (422), and (333) planes of cubic C_{60} (JCPDS: 79–1715) [22]. Fullerene exhibits a well-defined crystalline molecular structure in which C_{60} molecules are held together by van der Waals interactions [23–25].

For defective fullerene (Fig. 2b), the sharp diffraction peaks of pristine C_{60} significantly decreased in intensity and broadened, indicating partial loss of crystallinity and disruption of the molecular crystal lattice. New diffraction peaks appeared at 2θ = 9.04°, 18.51°, 20.01°, 21.69°, 26.92°, and 31.30°, and additional reflections at 35.32°, 47.98°, and 64.29° were observed, which were absent in pristine fullerene. The

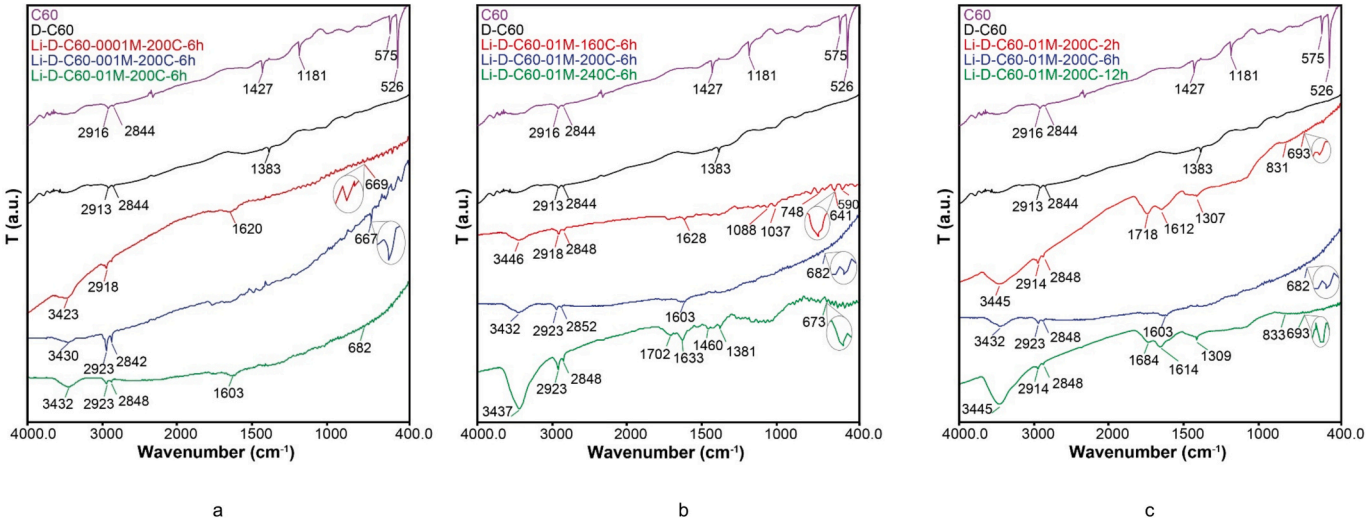

Fig. 1. FTIR spectra of C60, D—C60, and Li-doped defective fullerenes: (a) at different concentrations, (b) at different temperatures, and (c) at different times.

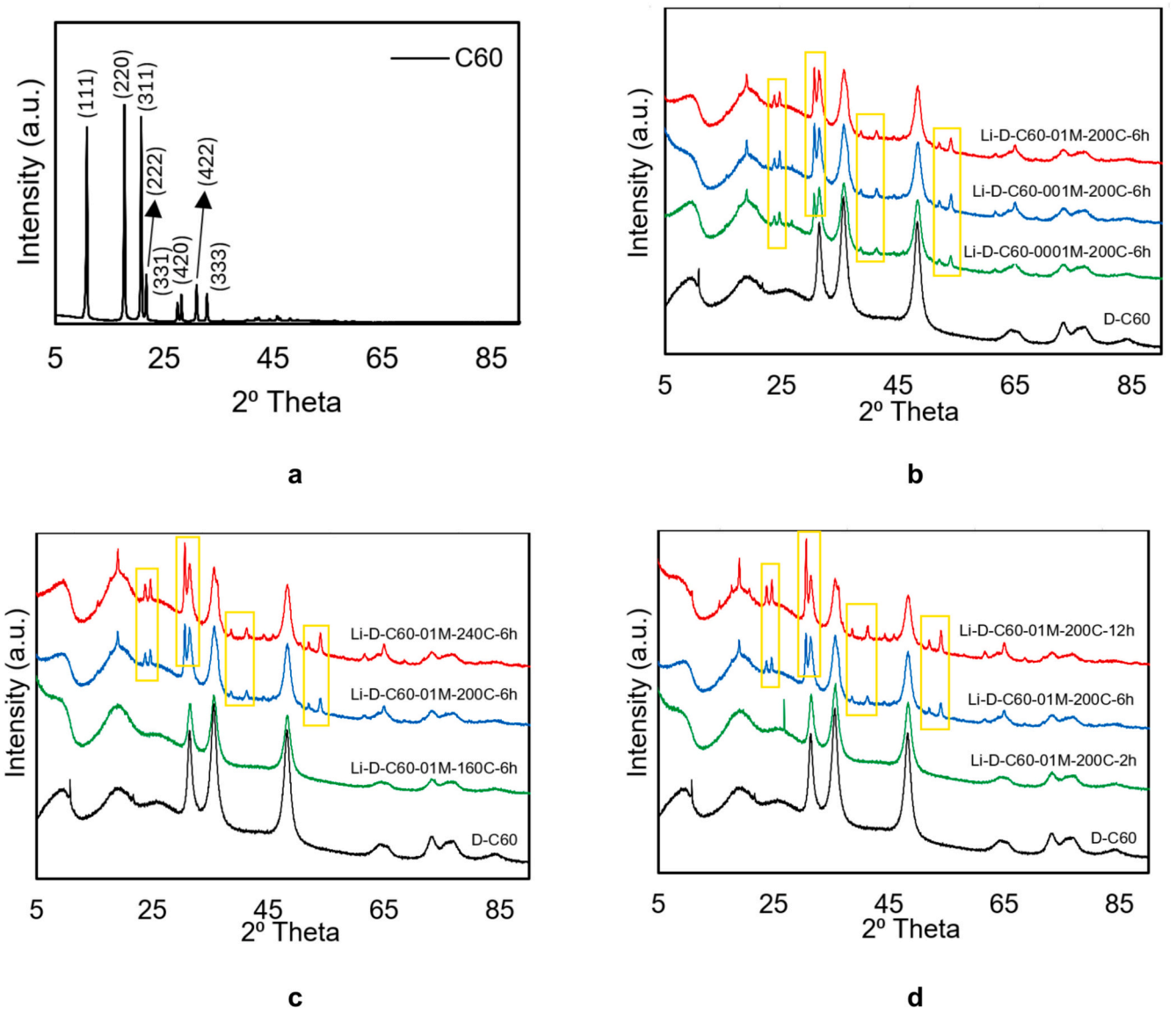

Fig. 2. XRD patterns of a) C60, b) D—C60 and Li-doped D—C60 samples at different concentrations, c) D—C60 and Li-doped D—C60 samples at different temperatures, and d) D—C60 and Li-doped D—C60 samples at different times.

reduction and broadening of diffraction peaks indicate a transition toward an amorphous structure and increased structural disorder [15].

The standard diffraction pattern of metallic lithium exhibits a body-centered cubic (BCC) structure, with characteristic peaks at $2\theta = 32.0°$, 52.3°, and 67.2° corresponding to the (110), (200), and (211) planes (JCPDS: 15–0401) [26]. Upon increasing Li concentration, peak intensities increased and additional reflections appeared at ~26–28°, 42–44°, ~52°, ~54°, and ~ 67°, indicating the formation of Li-containing crystalline phases and enhanced structural ordering.

The effect of temperature on Li doping (Fig. 2c) reveals that the sample synthesized at 160 °C exhibits a predominantly amorphous character, whereas distinct crystalline peaks become more pronounced at 200 °C and 240 °C. The absence of Li-related peaks at 160 °C suggests insufficient incorporation of Li into the fullerene lattice. In contrast, the emergence of diffraction peaks at ~52°, ~54°, and ~ 67°, along with peak splitting at ~30.57° and 31.54°, confirms Li incorporation and partial recrystallization at higher temperatures.

Time-dependent Li doping (Fig. 2d) shows that 2 h treatment is insufficient for complete doping, as indicated by broad and low-intensity peaks without characteristic Li reflections. With increasing reaction time (6 and 12 h), peak intensities increased and additional reflections appeared at $2\theta = 38.82°$, 41.13°, 44.51°, 52.15°, and 53.89°, indicating progressive crystallization and Li incorporation. These diffraction features are consistent with those observed for samples synthesized at elevated temperatures.

Overall, Li doping induces partial recrystallization and structural ordering in defective fullerenes. Appropriate control of Li concentration, temperature, and reaction time enables the formation of more ordered crystalline domains within the defective fullerene framework. In particular, 0.01 M Li concentration, 200 °C, and 12 h reaction time yielded the most pronounced crystalline features, suggesting optimized defect–dopant co-engineering conditions.

3.1.3. DTA/TG analysis

Thermograms of fullerene, defective fullerene, and Li-doped defective fullerene samples recorded under an inert nitrogen atmosphere are shown in Fig. 3, and the corresponding thermal stability parameters are summarized in Table 1. Pristine fullerene exhibits a single-step decomposition at approximately 850 °C with a mass loss of 73.1%, resulting in amorphous carbon formation. Cataldo reported that fullerene displays remarkable thermal stability with negligible mass loss up to 1000 °C, confirming its intrinsic thermal robustness [27].

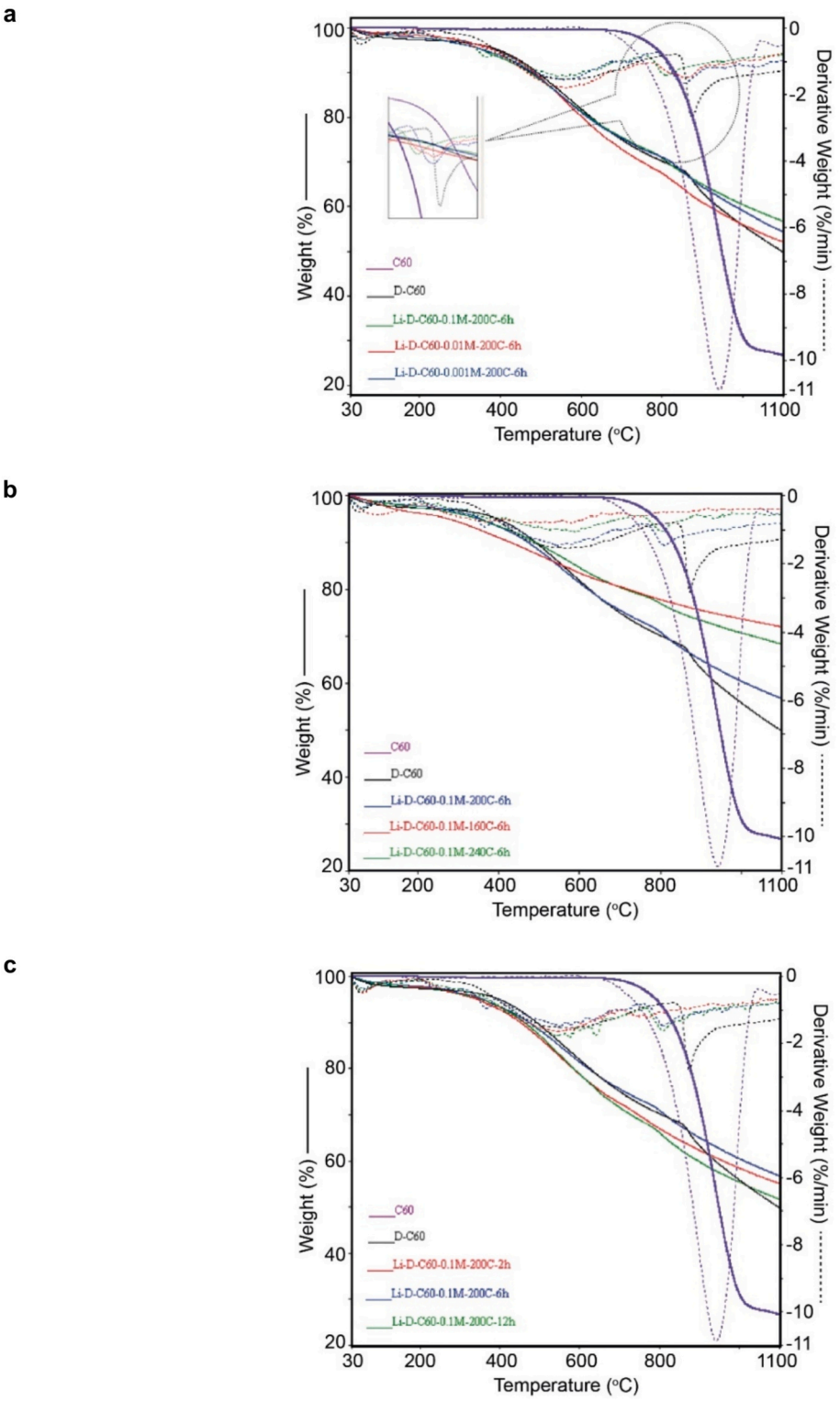

Fig. 3. TG and d[TG] thermograms of fullerene, defective fullerene and, Li-doped defective fullerene samples: at a) different concentrations, b) different temperatures and c) different times.

The formation of defective fullerene significantly reduced the thermal stability and introduced a two-step decomposition behavior. The first decomposition step occurs at 564 °C with a mass loss of 26.27%, followed by a second step at 848 °C with a mass loss of 17.75%. These results indicate that defect generation strongly alters the thermal decomposition pathway of fullerene by increasing structural disorder.

Li-doped defective fullerenes exhibit three-step thermal decomposition profiles, which are attributed to residual moisture, surface functional groups, and impurity phases introduced during hydrothermal doping. However, the main decomposition temperatures remain comparable to those of defective fullerene, suggesting that Li incorporation does not significantly compromise the high-temperature stability of the carbon framework.

The thermograms of Li-doped defective fullerene samples

Table 1
Thermal stability data obtained from TG and d[TG] analyses.

Samples	T_{max1} (°C)	ΔY (%)	T_{max2} (°C)	ΔY (%)	T_{max3} (°C)	ΔY (%)	Residue at 1100 °C (%)
C60	944.1	73.10	–	–	–	–	26.68
D-C60	564.3	26.27	848.1	17.75	–	–	49.85
Li-D-C60–0.1 M-200C-2 h	61.7	2.010	593.3	24.90	740.2	17.67	55.12
Li-D-C60–0.1 M-200C-6 h	64.3	2.09	575.1	24.78	810.2	16.32	56.73
Li-D-C60–0.1 M-200C-12 h	59.1	2.60	578.5	28.21	810.0	17.49	51.68
Li-D-C60–0.001 M-200C-6 h	65.4	1.49	573.0	29.30	865.3	16.92	52.10
Li-D-C60–0.01 M-200C-6 h	59.3	2.06	541.6	26.85	812.4	17.04	54.35
Li-D-C60–0.1 M-160C-6 h	101.2	3.72	480.0	15.25	733.2	8.88	72.03
Li-D-C60–0.1 M-240C-6 h	60.6	2.64	595.5	18.40	803.0	10.73	68.34

synthesized at different Li concentrations are presented in Fig. 3a. The first decomposition step occurs in the range of 59–65 °C, the second step between 573 and 593 °C, and the third step between 810 and 865 °C for Li-D-C60–01 M-200C-6 h, Li-D-C60–001 M-200C-6 h, and Li-D-C60–0001 M-200C-6 h samples. The residue at 1100 °C ranges from 52 to 57%. These results indicate that Li concentration has a limited effect

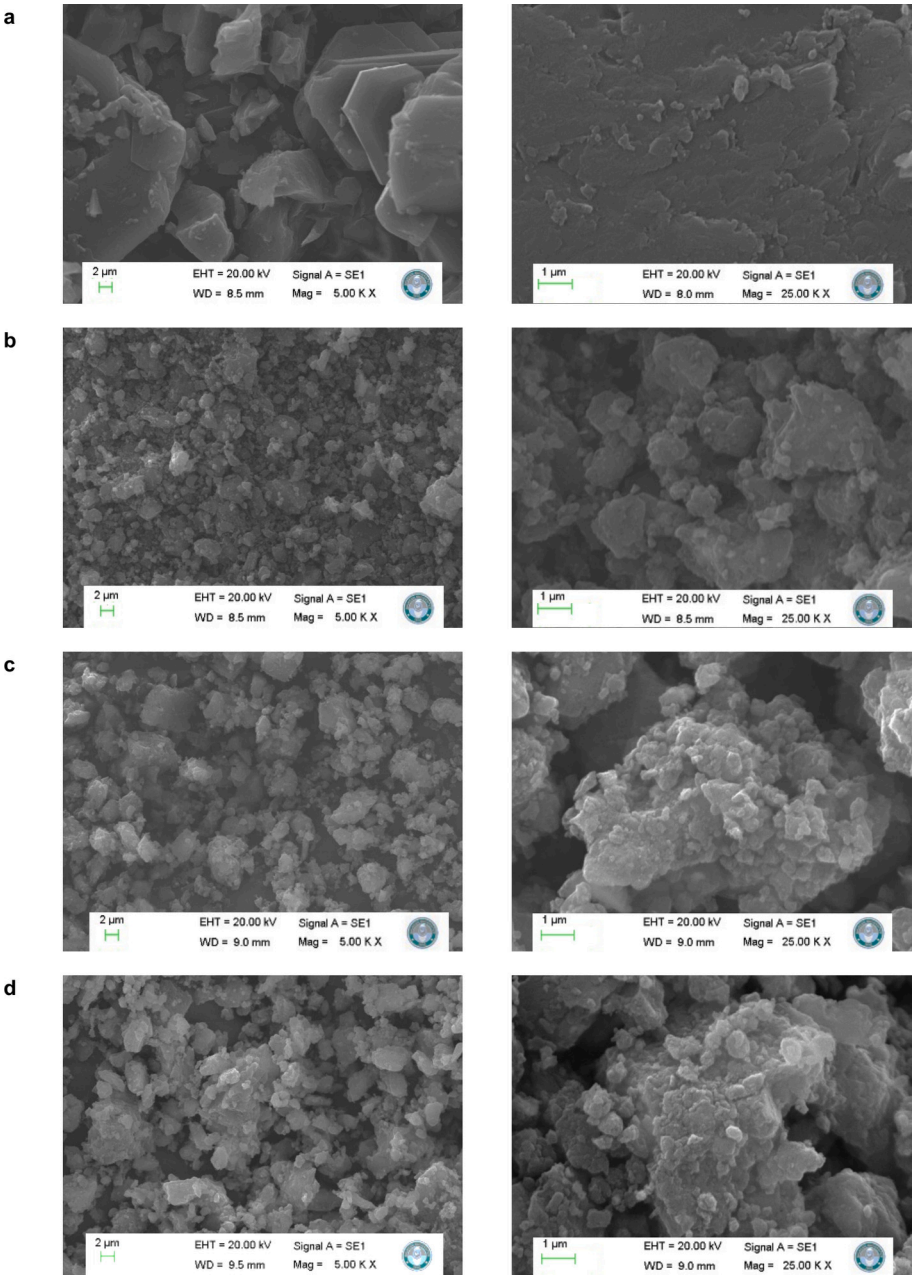

Fig. 4. SEM images of a) C60, b) D—C60, c) Li-D-C60–0001 M-200C-6 h, d) Li-D-C60–001 M-200C-6 h, e) Li-D-C60–01 M-200C-6 h f) Li-D-C60–01 M-160C-6 h, g) Li-D-C60–01 M-240C-6 h, h) Li-D-C60–01 M-200C-2 h and i) Li-D-C60–01 M-200C-12 h samples.

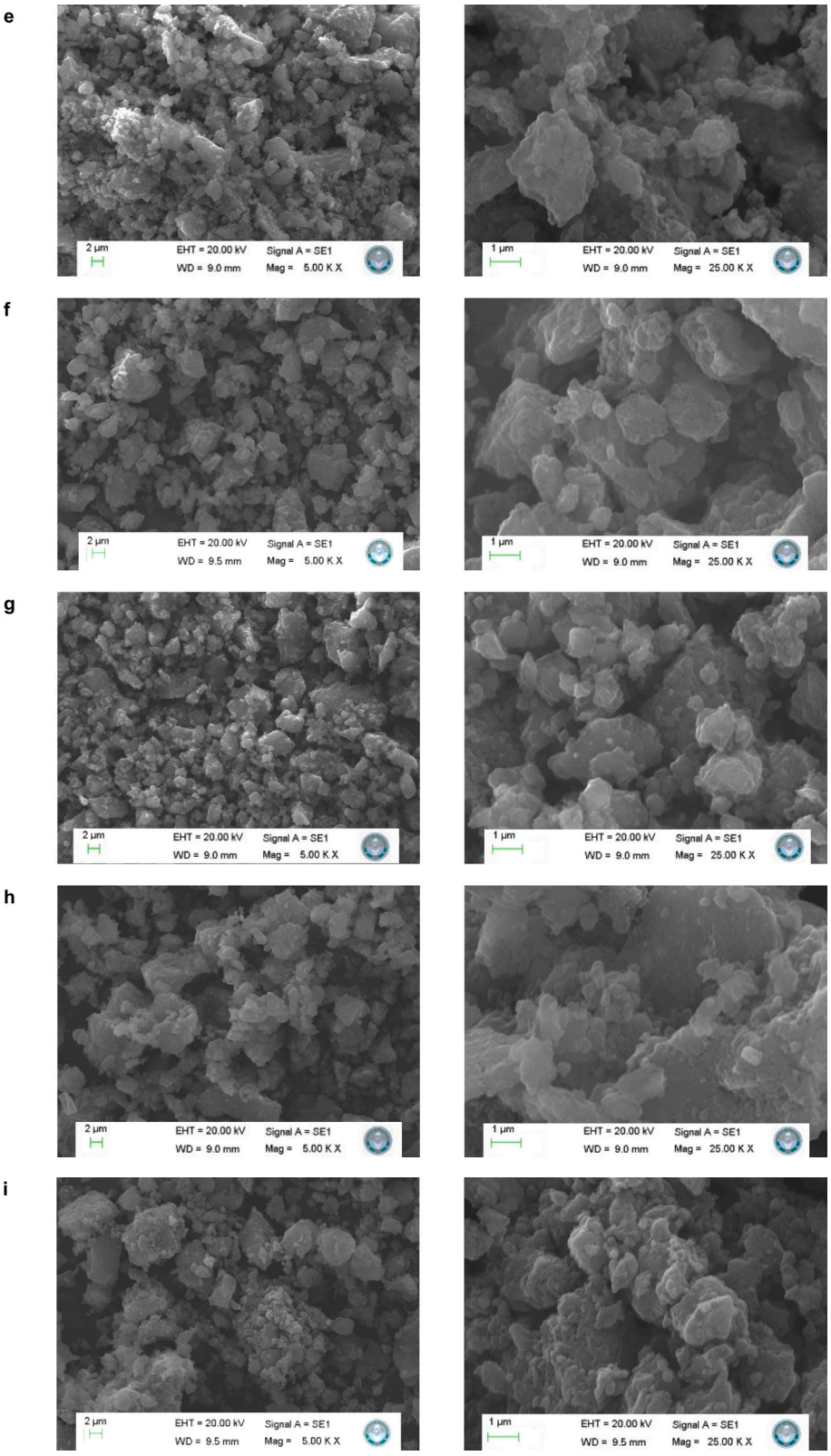

Fig. 4. (*continued*).

on the overall thermal stability of defective fullerene.

Similarly, the Li-doped samples prepared at different temperatures (Li-D-C60–01 M-160C-6 h, Li-D-C60–01 M-200C-6 h, and Li-D-C60–01 M-240C-6 h) show three decomposition stages occurring at 60–101 °C, 480–595 °C, and 733–810 °C, respectively (Fig. 3b and Table 1). The residual mass at 1100 °C varies between 56 and 72%. This indicates that the hydrothermal temperature has only a minor influence on the high-temperature stability of Li-doped defective fullerenes.

For the samples synthesized at different reaction times (Li-D-C60–01 M-200C-2 h, Li-D-C60–01 M-200C-6 h, and Li-D-C60–01 M-200C-12 h),

the first decomposition step occurs at 59–64 °C, the second step at 575–593 °C, and the third step at 740.2–810 °C (Fig. 3c). The residue values at 1100 °C are similar, ranging from 51 to 56%. These findings suggest that reaction time does not significantly alter the thermal stability once Li incorporation and defect formation are achieved.

3.1.4. SEM/EDX analysis

SEM images of Li-doped defective fullerene samples synthesized at different concentrations, temperatures, and reaction times are presented in Fig. 4. Pristine fullerene molecules form nanostructured particles that strongly agglomerate due to van der Waals interactions, often producing bulk microcrystalline aggregates, which makes individual particle size determination challenging [28]. The surface morphology of pristine fullerene (Fig. 4a) consists of irregular agglomerates with microcrystalline features and exhibits a relatively smooth and homogeneous surface compared to other samples.

Ball milling-induced defect formation significantly reduced the particle size and disrupted the crystalline structure, resulting in a more amorphous morphology for defective fullerene [15]. Lithium doping further modified the surface morphology, leading to larger particle aggregates compared to defective fullerene, regardless of doping concentration, temperature, or reaction time. This aggregation behavior can be attributed to chemical doping effects and high-temperature hydrothermal treatment, which promote particle coalescence and surface adhesion of smaller particles onto larger clusters.

At low Li concentrations, a pronounced agglomeration tendency was observed (Figs. 4c and d), whereas increasing Li concentration reduced clustering and produced a more dispersed morphology (Fig. 4e). It should be noted that SEM provides lateral surface distribution information, whereas AFM characterizes vertical topography; therefore, SEM and AFM analyses provide complementary insights into surface morphology. The reduced agglomeration at higher Li concentrations suggests enhanced particle dispersion due to improved Li integration within the fullerene framework.

Temperature-dependent doping experiments revealed that agglomeration decreased with increasing hydrothermal temperature (Figs. 4e–g), indicating improved crystallization and particle redistribution at elevated temperatures. Similarly, reaction time strongly influenced morphology: the sample synthesized for 2 h exhibited severe clustering, whereas extended reaction times (6 h and 12 h) resulted in more homogeneous and less agglomerated structures (Figs. 4h–i). The Li-D-C60–01 M-200C-12 h sample showed the most uniform morphology and exhibited the highest hydrogen storage capacity, suggesting a correlation between surface homogeneity and hydrogen adsorption–diffusion efficiency.

The EDX spectra and elemental distribution maps are shown in Fig. S.1 (Supplementary Material), and the elemental compositions are summarized in Table 2. Au/Pd coating was applied to enhance surface conductivity; therefore, Au and Pd peaks at ~9.71 keV and ~ 2.84 keV were excluded from compositional analysis [29]. The EDX results reveal that pristine fullerene consists predominantly of carbon (97.36 wt%) with minor oxygen content (2.64 wt%). Defective fullerene exhibited reduced carbon content (82.60 wt%) and increased oxygen content (9.76 wt%), attributed to oxidation during ball milling, as previously reported for carbonaceous materials [30]. Additionally, trace amounts of W, Cu, and Co were detected, originating from tungsten carbide milling media contamination [15].

Lithium doping resulted in a systematic decrease in carbon content and an increase in oxygen content, indicating enhanced surface oxidation during hydrothermal treatment. Increasing Li concentration promoted greater oxygen incorporation, whereas increasing hydrothermal temperature led to higher carbon content and reduced oxygen content, likely due to enhanced carbonization under hydrothermal conditions. Longer reaction times increased oxygen content, suggesting progressive surface oxidation.

Because EDX is insufficient for detecting light elements such as lithium, XPS analysis was performed. The XPS spectra (Fig. 5) show only C 1 s (~282 eV) and O 1 s (~531 eV) peaks for C60 and D—C60 samples, whereas a distinct Li 1 s peak at ~53 eV appears exclusively in Li-D-C60 samples, confirming successful Li incorporation into the defective fullerene structure.

3.1.5. TEM images

In the literature, the diameter of individual fullerene molecules is reported to be approximately 0.7 nm [15]. However, due to strong van der Waals interactions, fullerene molecules tend to form agglomerates with significantly larger dimensions. TEM images of fullerene and defective fullerene are presented in Fig. 6 and reveal distinct morphological features.

As shown in Fig. 6a, fullerene particles appear as aggregated clusters with sizes ranging from 50 to 150 nm, indicating pronounced agglomeration behavior. The observed dark regions correspond to areas with higher electron scattering, typically associated with thicker or denser particle domains. The predominantly spherical or oval particle morphology reflects the intrinsic symmetry of fullerene cage structures.

Fig. 6b demonstrates that mechanical milling induces significant structural disruption in fullerene aggregates. The presence of both dark (larger agglomerates) and lighter (dispersed or fragmented) regions indicates heterogeneous particle size distribution after milling. While some fullerene domains preserve their original morphology, others exhibit symmetry loss and fragmentation, confirming the formation of defective fullerene structures. Such defect generation is expected to significantly affect textural properties, including BET surface area and pore volume, and to increase surface reactivity, thereby enhancing their suitability for adsorption-based applications.

3.1.6. AFM analysis

Topographical characterization of C60, D—C60, and Li-doped defective fullerenes was carried out using AFM to evaluate the surface roughness and height profiles of the samples. The 2D and 3D topographies obtained using Nanosurf software are presented in Fig. 7. As

Table 2
wt% elemental compositions of C60, D—C60 and Li-doped defective fullerene samples.

Samples	C (wt%)	O (wt%)	W (wt%)	Cu (wt%)	Co (wt%)
C60	97.36	2.64	–	–	–
D-C60	82.60	9.76	5.17	2.13	0.35
Li-D-C60–0.001 M-200C-6 h	82.95	10.46	5.33	1.48	0.48
Li-D-C60–0.01 M-200C-6 h	80.66	10.45	6.75	1.57	0.57
Li-D-C60–0.1 M-200C-6 h	80.40	11.96	5.21	2.44	–
Li-D-C60–0.1 M-160C-6 h	78.85	17.11	2.30	1.74	–
Li-D-C60–0.1 M-240C-6 h	81.81	9.67	5.73	2.30	0.48
Li-D-C60–0.1 M-200C-2 h	79.30	14.40	4.06	2.24	–
Li-D-C60–0.1 M-200C-12 h	78.20	15.45	4.04	2.30	–

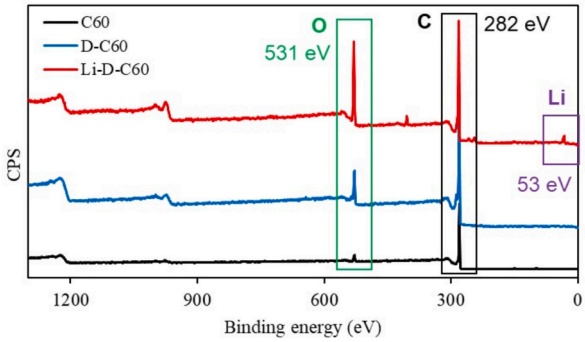

Fig. 5. XPS spectra of C60, D—C60 and Li-D-C60.

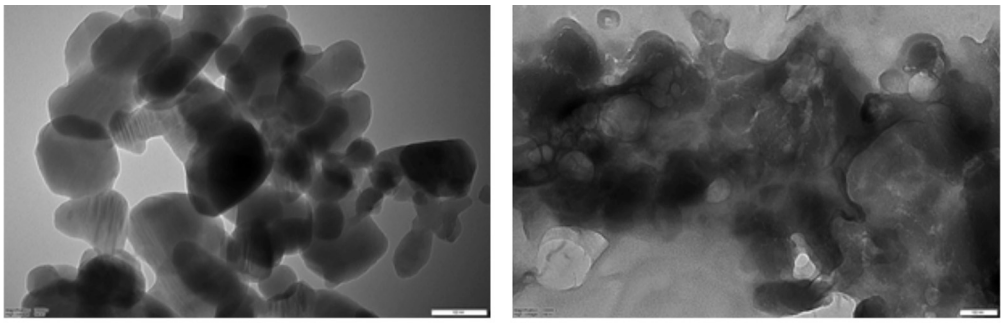

Fig. 6. TEM images of a) C60 and b) D—C60.

shown in Fig. 7a, pristine fullerene exhibits surface height variations reaching up to ~1 μm, which can be attributed to the formation of large agglomerates driven by van der Waals interactions between C60 molecules. Literature reports randomly arranged bulk, sphere-like aggregates of fullerene molecules with diameters ranging from a few nanometers to several hundred nanometers, consistent with the present observations [31–33].

Fig. 7b demonstrates that mechanical milling significantly reduces particle size and surface protrusions in defective fullerenes, with the maximum topographical height decreasing from ~1 μm to ~47 nm. This indicates that defect formation disrupts agglomerates and enhances particle dispersion. Figs. 7c–i show the 2D and 3D topographies of Li-doped defective fullerene samples prepared under different concentrations, temperatures, and reaction times. The Li-doped samples display more pronounced and heterogeneous surface features, with topographical heights increasing from 0.62 μm to a maximum of 0.93 μm, suggesting that lithium incorporation promotes particle re-aggregation and increases surface roughness. However, no clear systematic dependence of topographical height on concentration, temperature, or reaction time was observed.

Overall, the observed variations in AFM images mainly reflect changes in surface roughness and particle size distribution, indicating that Li doping and hydrothermal processing significantly influence surface morphology. Lithium doping substantially alters the surface topography of defective fullerenes: lower Li concentrations (0.001 M) yield relatively homogeneous surfaces, whereas higher dopant levels lead to increased height variations and spherical agglomerate-like features. Reaction temperature and time also affect surface morphology; treatment at 200 °C for 6 h produces relatively uniform surface features, whereas higher temperatures (240 °C) and prolonged reaction times (12*h*) promote larger clusters, while shorter times (2 h) result in smoother surfaces with smaller features.

It should be noted that AFM-derived height variations represent vertical surface roughness rather than lateral particle agglomeration. Therefore, the term “agglomeration” in AFM refers to vertical surface protrusions, whereas SEM observations describe horizontal particle clustering. Because AFM and SEM probe different morphological dimensions, their results are complementary rather than contradictory.

3.2. EIS analysis

Electrochemical impedance spectroscopy (EIS) analyses, conducted to evaluate the interfacial charge-transfer and diffusion characteristics of the electrode materials, are shown in Fig. 8. Nyquist diagrams depict the responses of C60, D—C60, and the Li-doped defective fullerene samples synthesized at various concentrations, temperatures, and reaction times. When both Z' and $-Z''$ components are examined, all samples exhibit similar slopes with nearly linear impedance profiles, indicating that the electrochemical behavior is predominantly governed by diffusion-controlled processes (Warburg-type behavior) rather than purely capacitive responses. Yalçınkaya et al. (2024) demonstrated that ion-diffusion kinetics dominate the electrochemical process in MWCNT and functionalized MWCNT electrodes [17]. Accordingly, the present system can be described as a mixed diffusion–semiconductor-controlled electrochemical system rather than an ideal capacitive electrode [34].

Introducing structural defects into the C60 lattice (D—C60) increases the overall impedance, suggesting a decrease in electrical conductivity due to lattice disorder. This trend is consistent with FTIR results, which indicate disruption of the C—C bonding framework. Lithium doping, particularly at 0.1 M Li concentration, 200 °C processing temperature, and a 6 h hydrothermal reaction, significantly reduce impedance and improves charge transport. SEM and AFM analyses indicate that samples synthesized under these conditions exhibit relatively homogeneous surface morphologies, which may facilitate ion/electron transport pathways. The appearance of Li—O vibrational bands in FTIR spectra further confirms the successful incorporation of lithium into the defective fullerene structure.

The dependence of impedance on temperature and reaction time suggests that Li doping is sensitive to both kinetic and thermodynamic parameters. The higher impedance observed for samples synthesized at 240 °C may be associated with increased lattice disorder or structural rearrangements at elevated temperatures, which can hinder charge-carrier mobility. Similarly, the increased impedance in samples doped for 12 h may indicate excessive Li accumulation or the formation of diffusion-blocking regions. The consistency between EIS trends and BET/hydrogen-storage results suggests that improved electronic conductivity contributes to enhanced hydrogen adsorption performance. Overall, these findings demonstrate that Li-doped defective fullerenes exhibit tunable electrochemical and interfacial properties, highlighting their potential as functional carbon-based materials for hydrogen storage applications.

The impedance spectra were fitted using a Randles equivalent circuit (Rs–(Rct + Zw) ‖ Cd), where Rs is the solution resistance, Cd is the double-layer capacitance, Rct is the charge-transfer resistance, and Zw represents the Warburg diffusion impedance (Fig. 8). In impedance spectra, the semicircle observed at high frequencies corresponds to the electron-transfer-limited process, while the linear region at low frequencies reflects diffusion-controlled behavior [35]. As summarized in Table 3, Rct values range from 0.07 to 0.11 kΩ, with pristine C60 exhibiting the lowest Rct (0.07 kΩ) and D—C60 the highest (0.11 kΩ). Most Li-doped defective fullerene samples show intermediate Rct values (0.08–0.10 kΩ), indicating efficient charge-transfer characteristics. Lithium doping slightly decreases Rct compared to D—C60, suggesting enhanced ion/electron transport, whereas variations in synthesis temperature and reaction time do not significantly influence Rct values.

3.3. Hydrogen storage

The hydrogen storage capacities of pure fullerene, defective fullerene, and defective fullerene samples doped with lithium at

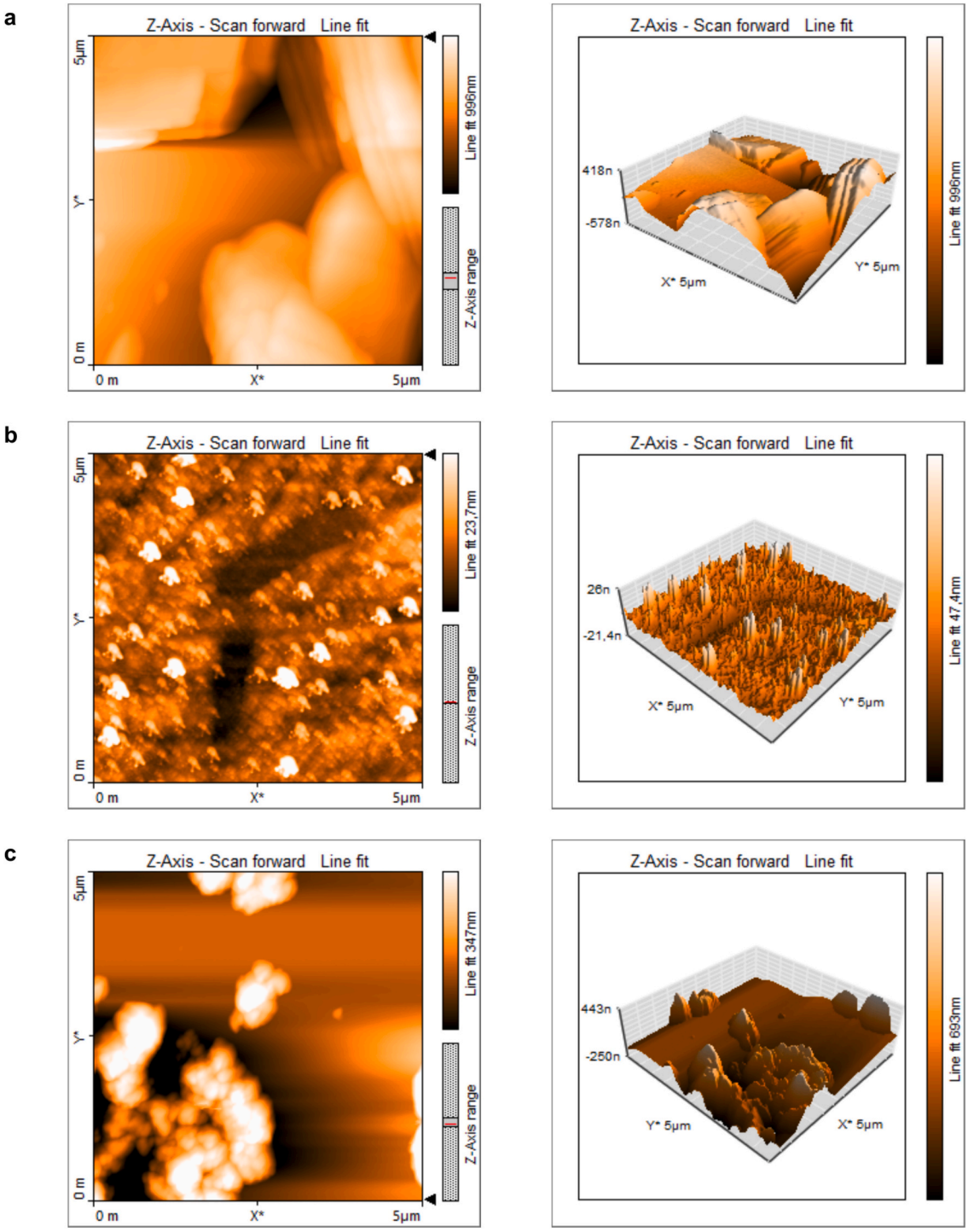

Fig. 7. 2D and 3D topography of a) C60, b) D—C60, c) Li-D-C60–0001 M-200C-6 h, d) Li-D-C60–001 M-200C-6 h, e) Li-D-C60–01 M-200C-6 h f) Li-D-C60–01 M-160C-6 h, g) Li-D-C60–01 M-240C-6 h, h) Li-D-C60–01 M-200C-2 h ve i) Li-D-C60–01 M-200C-12 h samples.

different concentrations, temperatures, and reaction times using the hydrothermal method were measured at room and cryogenic temperatures as a function of pressure. As seen in Fig. 9, the isotherm curves at these two temperature regimes exhibit distinct behaviors. The amount of hydrogen adsorbed at room temperature shows a strictly linear relationship with increasing pressure, primarily because the active sites and pores on the fullerene surfaces remain unoccupied. This linearity indicates that adsorption is not limited by saturation of a finite number of specific sites within the investigated pressure range, and therefore additional uptake remains possible as pressure increases. Another factor contributing to the linear increase in hydrogen storage with rising pressure is the corresponding increase in hydrogen gas density, which enhances its interaction with fullerene surfaces and pores [19].

The increase in the amount of hydrogen stored with pressure at room temperature is also consistent with Henry's law, which states that the amount of a gas adsorbed on a solid surface or within its pores under low pressures varies directly with the gas pressure [36,37]. A similar trend was observed for hydrogen adsorption on NaA zeolites. Monte Carlo

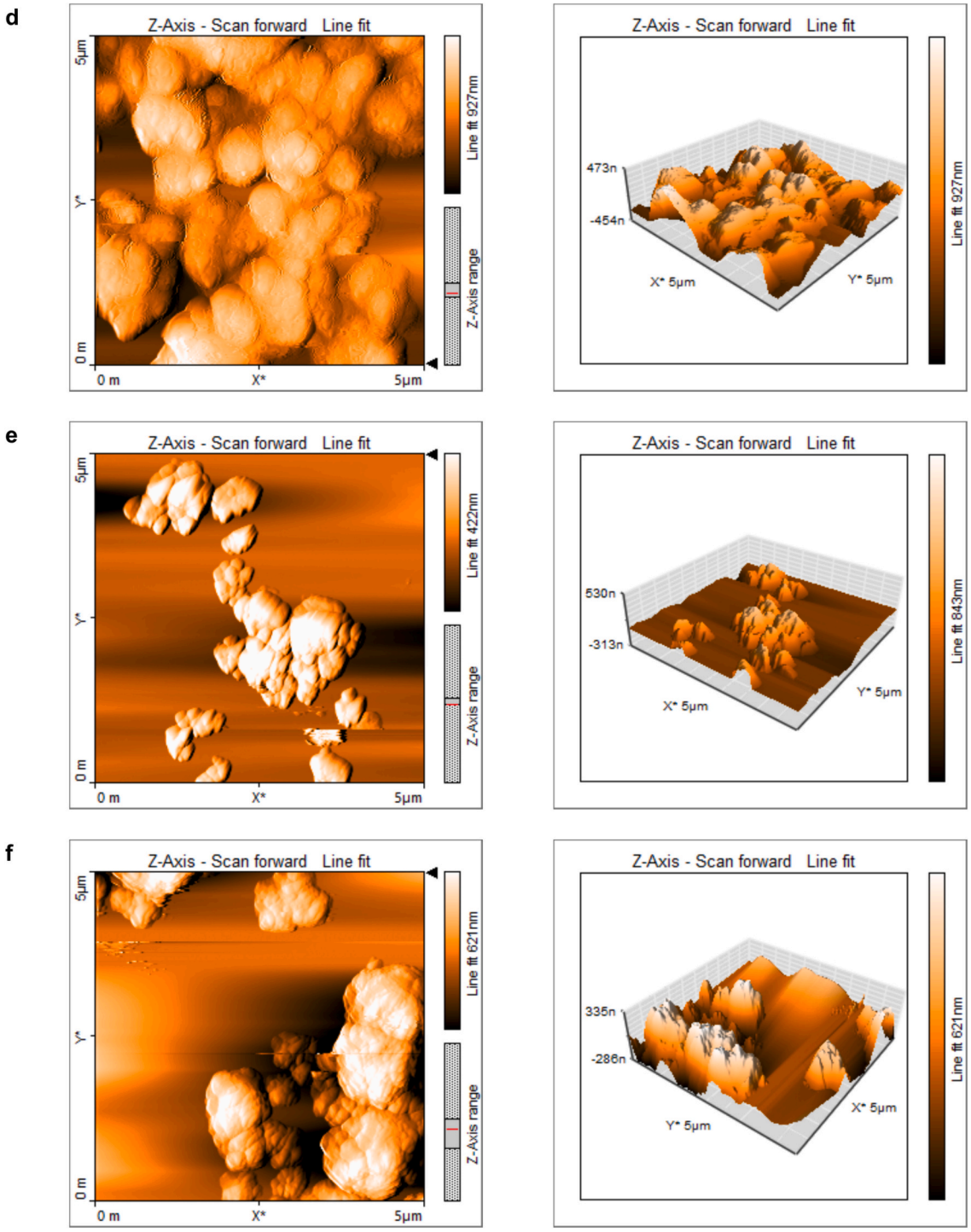

Fig. 7. (*continued*).

simulations performed at different temperatures and pressure ranges demonstrated that the adsorbed amount increases proportionally with pressure, in agreement with Henry's law [36]. Likewise, in zeolite-templated carbon materials, particularly at 298 K, the amount of hydrogen stored under a given pressure also increased linearly [37].

At cryogenic temperature, it is observed that the hydrogen storage capacities of the doped samples, except for C60 and D—C60, increase with pressure, then reach a maximum without forming a plateau, decrease with further pressure increase, and subsequently begin to rise again as the pressure continues to increase. This behavior can be explained by excess adsorption. The excess adsorption values for Li-D-C60–01 M-200C-6 h, Li-D-C60–001 M-200C-6 h, Li-D-C60–0001 M-200C-6 h, Li-D-C60–01 M-160C-6 h, Li-D-C60–01 M-240C-6 h, Li-D-C60–01 M-200C-2 h, and Li-D-C60–01 M-200C-12 h were 0.669, 0.624, 0.565, 0.780, 0.692, 0.800, and 0.870 wt% at pressures of 18.24, 27.48, 21.91, 18.81, 15.16, 18.19, and 18.19 bar, respectively. These results show that the lithium-doped samples exhibit excess adsorption behavior in the pressure range of 15.16–27.48 bar. The highest excess adsorption value was determined for Li-D-C60–01 M-200C-12 h, which has the highest BET surface area and micropore volume. Excess adsorption refers to the storage of an adsorbate within the cavities of a porous adsorbent under specific temperature and pressure conditions. In this

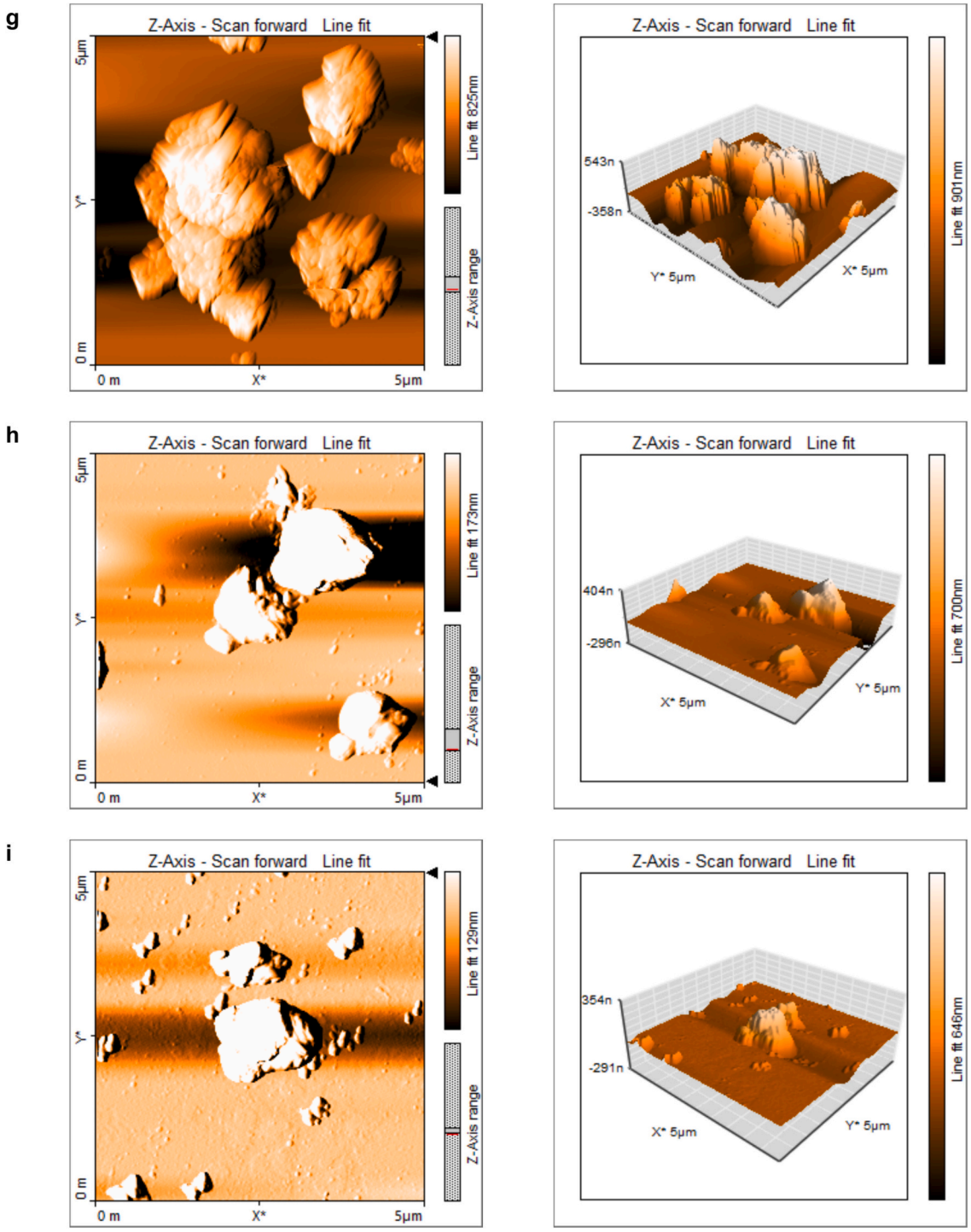

Fig. 7. (*continued*).

phenomenon, the adsorbate does not fully occupy the entire pore volume but is partially retained within these cavities. This process occurs due to the density of the gas-phase adsorbate and its interaction with the pore surfaces [38]. Accordingly, the observed maximum in excess adsorption reflects a balance between increasing adsorbed-phase density and the definition of "excess" relative to the bulk gas density at cryogenic conditions. Excess adsorption under high pressure enables more gas molecules to interact with the adsorbent surface, thereby increasing the total amount adsorbed. C60 and D—C60 samples exhibit multilayer adsorption behavior. These results, consistent with SEM analysis, indicate that Li-doping induces morphological changes in the samples. Hydrogen storage in these structures occurs predominantly through van der Waals interactions. During this process, lithium atoms provide additional binding sites by creating electrostatic interaction regions on both the surface and interior of the fullerene structures. These sites enhance the adsorption of hydrogen molecules, leading to higher storage capacities [39]. Importantly, the hydrogen release pathway reveals an additional practical advantage beyond capacity enhancement: the Li-doped centers can act as controllable "hydrogen release valves", enabling a safer, more controlled, and reversible desorption process compared with pristine fullerene. Similar findings were reported in hydrogen storage isotherm curves of activated carbon samples produced

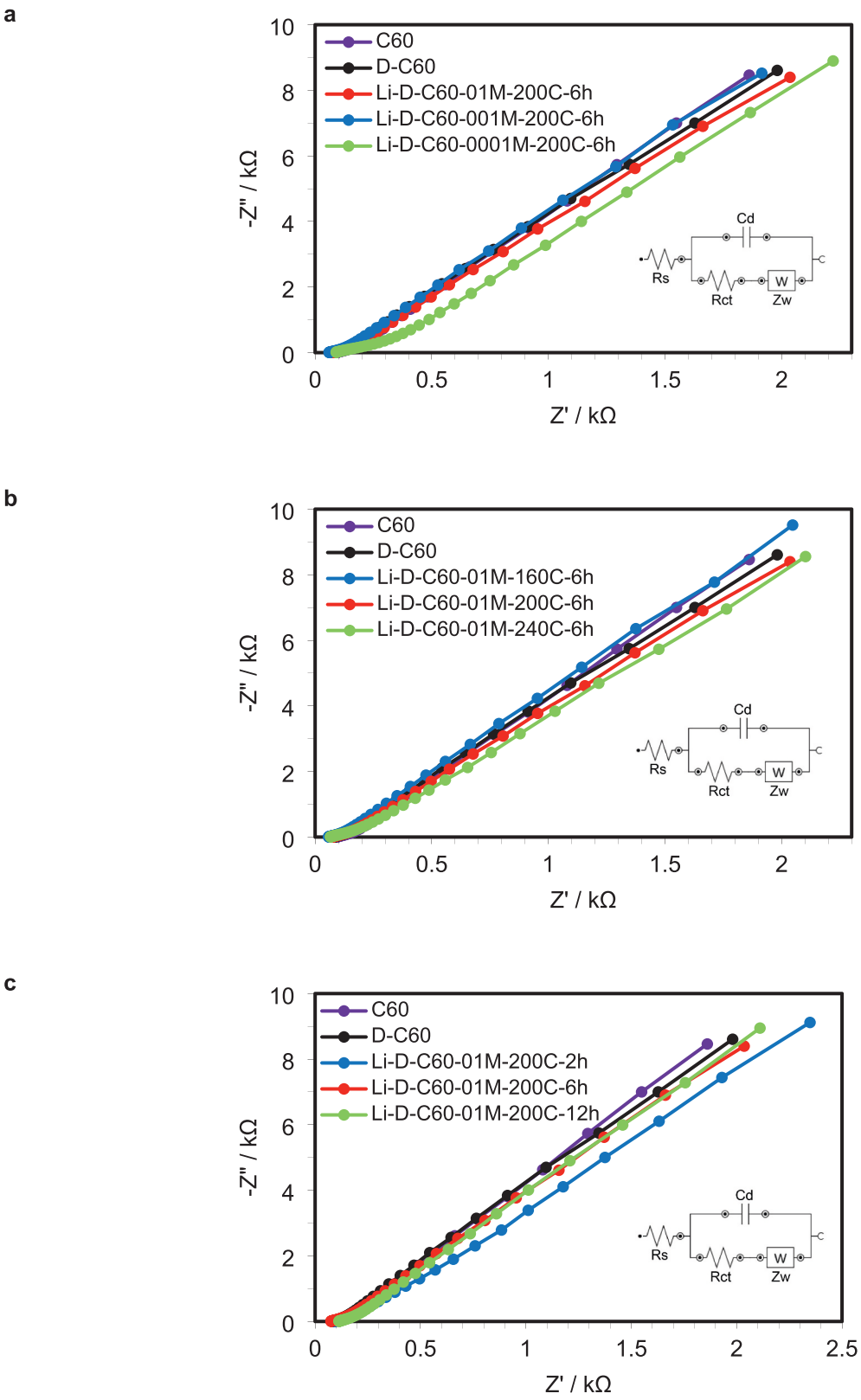

Fig. 8. Nyquist plots of C60, D—C60, and the defective fullerenes doped with lithium at a) different concentrations, b) different temperatures and c) different times.

from tangerine peel using different activation agents followed by carbonization at various temperatures [40]. In addition, experiments on IRMOF-1 demonstrated that the maximum excess hydrogen adsorption, approximately 9 wt%, was obtained at 50 K and 10 bar. The experimental data showed that at low temperatures, excess adsorption isotherms reached a maximum and subsequently decreased rapidly. Furthermore, excess adsorption at 50 K yielded an adsorbed phase with a density significantly higher than that of the gas phase [41]. In another study, the excess adsorption isotherms of metal–organic frameworks (MOFs) with rht topology were investigated. Experimental results

Table 3
BET surface area, pore volume and charge-transfer resistance data of C60, D—C60 and Li-doped defective fullerene samples.

Samples	S_{BET} (m^2/g)	V_t (cc/g)	V_{micro} (cc/g)	V_{dft} (cc/g)	V_{meso} (cc/g)	V_{macro} (cc/g)	Rct (kΩ)
C60	61.74	0.0533	0.009	0.0451	0.0361	0.0172	0.07
D-C60	168.9	0.1723	0.072	0.1509	0.0789	0.0214	0.11
Li-D-C60–0.001 M-200C-6 h	206.20	0.148	0.087	0.132	0.045	0.016	0.10
Li-D-C60–0.01 M-200C-6 h	200.40	0.155	0.084	0.137	0.053	0.018	0.08
Li-D-C60–0.1 M-200C-6 h	218.78	0.168	0.091	0.148	0.057	0.020	0.10
Li-D-C60–0.1 M-160C-6 h	211.15	0.139	0.093	0.123	0.030	0.016	0.09
Li-D-C60–0.1 M-240C-6 h	214.84	0.163	0.095	0.150	0.055	0.013	0.10
Li-D-C60–0.1 M-200C-2 h	217.57	0.154	0.092	0.135	0.043	0.019	0.09
Li-D-C60–0.1 M-200C-12 h	239.80	0.155	0.099	0.135	0.036	0.020	0.11

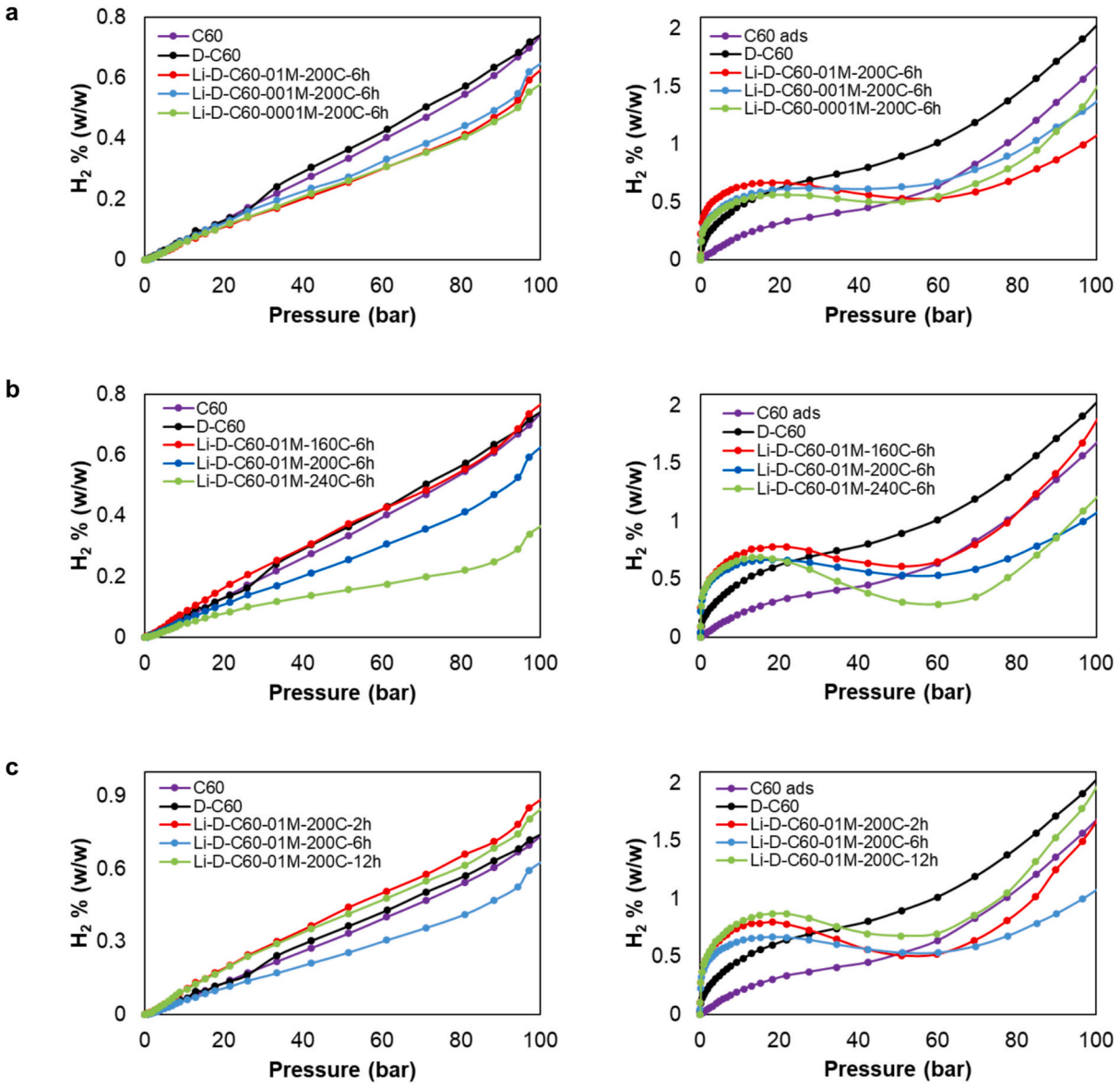

Fig. 9. Hydrogen storage capacities of C60, D—C60 and a) Li-D-C60–01 M-200C-6 h, Li-D-C60–001 M-200C-6 h and Li-D-C60–0001 M-200C-6 h; b) Li-D-C60–01 M-160C-6 h, Li-D-C60–01 M-200C-6 h and Li-D-C60–01 M-240C-6 h; and c) Li-D-C60–01 M-200C-2 h, Li-D-C60–01 M-200C-6 h and Li-D-C60–01 M-200C-12 h at room and cryogenic temperatures.

showed that MOFs with similar compositions, such as NOTT-116 and PCN-68, exhibited comparable hydrogen adsorption isotherms, but the maxima in their **excess** adsorption curves occurred at different pressures (~30 and ~ 46 bar). Additionally, the adsorbed amount in NOTT-116 decreased much more rapidly than in PCN-68 after reaching the maximum [38].

Fig. 9a shows the pressure-dependent hydrogen storage capacities of C60, D—C60, Li-D-C60–01 M-200C-6 h, Li-D-C60–001 M-200C-6 h, and Li-D-C60–0001 M-200C-6 h at both room and cryogenic temperatures. The figure demonstrates that the hydrogen storage capacities of the

fullerene-based samples differ significantly from one another. The hydrogen storage performance of solid adsorbents depends on their BET surface area and pore volume, particularly the micropore volume. According to IUPAC, there are six classifications describing the physical adsorption of gases on adsorbents, in which the pore structure of the adsorbent plays a critical role. The isotherm curves obtained from N_2 adsorption–desorption measurements for fullerene, defective fullerene, and Li-doped defective fullerenes are presented in Fig. S.2 (Supplementary Material). Except for pristine fullerene, defective fullerenes and Li-doped defective fullerenes display similar N_2 adsorption–desorption profiles. While fullerene shows low adsorption capacity at low P/P° values and a linear increase with rising P/P° ratio, defective fullerenes and Li-doped defective fullerenes exhibit notably higher adsorption capacities. In general, adsorption predominantly occurs within micropores at low P/P° values. The BET surface areas, total pore volumes (V_t), micropore volumes (V_{micro}), DFT pore volumes (V_{dft}), mesopore volumes (V_{meso}), and macropore volumes (V_{macro}) calculated from the N_2 adsorption–desorption isotherms are listed in Table 3. Additionally, the variations in cumulative pore volumes of fullerene, defective fullerene, and Li-doped defective fullerenes as a function of pore width are shown in Fig. S.3 (Supplementary Material). Fullerenes have very low BET surface area and pore volume, especially micropore volume. However, with the production of defective fullerene and Li-doped defective fullerenes, both the BET surface area and pore volumes, especially micropore volumes, increase. The reason for the low adsorption capacity of fullerene at low P/P° values is that both BET surface area and micropore volume are quite low. Fullerene exhibits a mesoporous structure. With the production of defective fullerene and Li-doped defective fullerene, significant increases occurred in BET surface areas and especially in micropore volumes. The high adsorption capacity of these samples at low P/P° values is due to their high micropore volumes. It is seen that all N_2 adsorption-desorption isotherms exhibit hysteresis in the range of $P/P^\circ = 0.3–1.0$. This is generally a situation observed in adsorbents with mesoporous structure. These results show that the N_2 adsorption-desorption isotherms of defective fullerene and Li-doped defective fullerene samples are in good agreement with Type 4 according to IUPAC classification [42]. The BET surface area of fullerene is 61.7 m^2/g, while the BET surface area of defective fullerene is 168.9 m^2/g. It is observed that the BET surface area of fullerene increases by 274% with the formation of defective structure. However, the same increase rate was not observed in hydrogen storage capacity. While a 191% increase in hydrogen storage capacity occurred at cryogenic temperature and 21.9 bar, no significant change occurred at room temperature. Total, micro-, meso- and macropore volumes of fullerene were measured as 0.053, 0.009, 0.036 and 0.008 cc/g, respectively, while those of D—C60 were measured as 0.172, 0.072, 0.079 and 0.021 cc/g, respectively. These results show that significant increases in pore volumes occur in parallel with the increase in BET surface area in the formation of defective fullerene from fullerene. The increase in total, micro-, meso- and macropore volumes are 325, 800, 219 and 263%, respectively. These results show that the increase in hydrogen storage capacity in the production of defective fullerene from fullerene is more consistent with the BET surface area result. In order to investigate the effect of Li-doping on the hydrogen storage capacity of the D—C60 sample, firstly the defective fullerene samples were doped with 15 mL of 0.1, 0.01 and 0.001 M LiNO3 solutions by hydrothermal method at 200 °C for 6 h. The hydrogen storage capacity of the Li-doped samples at different concentrations is generally higher than that of the C60 and D—C60 samples up to the excess adsorption pressure, while it decreases after these pressures. The higher storage capacity of doped samples is due to higher BET surface areas and micropore volumes. Because the BET surface areas of Li-D-C60–0001 M-200C-6 h, Li-D-C60–001 M-200C-6 h and Li-D-C60–01 M-200C-6 h are 206.2, 200.4 and 218.8 m^2/g, respectively, while their total, micro-, meso- and macropore volumes are 0.148, 0.087, 0.045 and 0.016 cc/g; 0.155, 0.084, 0.053 and 0.018 cc/g; and 0.168, 0.091, 0.057 and 0.020 cc/g, respectively. Increases of 30% and 26% in BET surface area and micropore volume of Li-D-C60–01 M-200C-6 h produced by lithium doping of defective fullerene were observed, respectively. In aqueous medium, $LiNO_3$ ionizes and dissociates into Li^+ and NO_3^- ions. Free NO_3^- ions can be released by converting into gaseous nitrogen oxides under the effect of temperature and pressure generated in the reactor. This leads to the formation of new pores in defective fullerene structures. As the lithium concentration increases, the contribution of nitrogen oxides to pore formation increases, while the amount of lithium released in the solution medium increases. As a result, it can be said that the BET surface area of defective fullerene samples doped at high $LiNO_3$ concentrations will increase [43]. Grand Canonical Monte Carlo (GCMC) simulation calculations have shown that significant improvements occur in the hydrogen storage performance of Li-FPGNs with increasing lithium doping ratio. As the doping ratio is increased, gravimetric hydrogen storage capacities also increase; for example, Li-FPGN720 reached 9.1% gravimetric capacity at 77 K and 1 bar conditions. Since more Li atoms fill the internal cavities of FPGNs at high doping ratios, smaller cavities and a more homogeneous structure are formed, which increases the physisorption capacity. Overall, careful optimization of the lithium doping ratio can increase the hydrogen storage capacity of Li-FPGNs by up to three times [44]. DFT calculations showed that lithium doping of fullerene-intercalated hexagonal boron nitride (h-BN) structures significantly increased the hydrogen storage capacity. In particular, the Li-doped C50-BN cage structure achieved a gravimetric hydrogen storage capacity of 6.86 wt% at 77 K and 100 bar pressure. This is almost twice the capacity of the undoped structures. Doping provides more binding points by strengthening the interaction of hydrogen with the surface and offers a more efficient storage solution by reducing energy requirements [39]. Another reason is the interaction of lithium atoms, which have lower molecular weight than carbon atoms and enter the structure through doping, with hydrogen molecules. According to DFT calculations, lithium atoms can create a negative charge on the surface by changing the electron distribution of fullerenes, similar to nanotubes, during the doping process. This negative charge can increase the capacity to attract hydrogen and create new hydrogen adsorption sites. Positively charged lithium atoms allow the adsorption of at least three hydrogen molecules for each atom. This increases the interaction energy with hydrogen molecules, thus increasing the storage capacity of hydrogen in fullerenes. As a result, increasing the lithium doping ratio and/or concentration allows hydrogen to be adsorbed more effectively and thus increases the total storage capacity [45]. Among the doped samples, the sample with the highest storage capacity up to the excess adsorption pressure is Li-D-C60–01 M-200C-6 h. This sample was used in the next temperature optimization studies since it has both higher BET surface area and micropore volume than the other doped samples. The hydrogen storage capacities of Li-doped defective fullerene samples at 160, 200 and 240 °C for 6 h using 0.1 M $LiNO_3$ at room and cryogenic temperatures are given in Fig. 9b. The hydrogen storage capacities of Li-doped samples at cryogenic temperature increase rapidly up to the excess adsorption pressure, while they increase linearly at room temperature. It is observed that the storage capacities decrease after the excess adsorption pressure point and increase again with increasing pressure. The storage capacities of the samples doped up to the excess adsorption pressure are higher than those of C60 and D—C60 samples.

As can be seen from Table 3, there was no significant change in the BET surface areas and pore volumes of Li-doped defective fullerene samples with increasing temperature. For example, the BET surface areas of Li-D-C60–01 M-160C-6 h, Li-D-C60–01 M-200C-6 h and Li-D-C60–01 M-240C-6 h were measured as 227.0, 218.8 and 224.7 m^2/g, respectively. Also, the micro-, meso- and macropore volumes of Li-D-C60–01 M-160C-6 h, Li-D-C60–01 M-200C-6 h and Li-D-C60–01 M-240C-6 h samples were 0.093, 0.030 and 0.016 cc/g; 0.091, 0.057 and 0.020 cc/g; and 0.095, 0.055 and 0.025 cc/g, respectively. Considering the fact that there is no significant change in both BET surface area and pore volume, the measured values are quite close to each other and the

production costs in terms of energy, the Li-D-C60–01 M-200C-6 h was selected for temperature optimization. The fact that no significant change occurred in the BET surface areas of Li-doped defective fullerene samples with the increase in temperature may be due to the fact that all NO_3^- ions in the aqueous medium are converted into free nitrogen monoxide gases in the range of 160-240 °C under the pressure that occurs spontaneously in the reactor. Since NO_3^- ions will produce approximately the same amount of nitrogen monoxide gases for the three samples, the change in BET surface areas is expected to be approximately the same.

The defective fullerene sample optimized with respect to concentration and temperature was doped with 0.1 M $LiNO_3$ at 200oC for 2, 6 and 12 h. The hydrogen storage capacities of C60, D—C60 and Li-doped defective fullerene samples at room and cryogenic temperatures are presented in Fig. 9c. At room temperature, the storage capacities of all samples increase linearly with pressure. At cryogenic temperature, the hydrogen storage capacities of the samples doped up to the excess adsorption pressure increase rapidly. The maximum increase in storage capacity up to excess adsorption pressure was observed for Li-D-C60–01 M-200C-12 h doped with lithium for 12 h. The BET surface areas of Li-D-C60–01 M-200C-2 h, Li-D-C60–01 M-200C-6 h and Li-D-C60–01 M-200C-12 h were measured as 221.9, 218.8 and 239.8 m^2/g, respectively. Micro-, meso- and macropore volumes were calculated as 0.092, 0.043 and 0.019 cc/g; 0.091, 0.057 and 0.020; and 0.099, 0.036 and 0.020 cc/g, respectively. These results show that both BET surface area and micropore volume increase slightly with increasing doping time. This may be due to the contribution of NO_3^- ions to micropore formation by entering into the inner parts of defective fullerenes with longer doping times. Because both BET surface area and micropore volume of Li-D-C60–01 M-200C-12 h increased. These results indicate that Li-D-C60–01 M-200C-12 h, which is one of the samples obtained as a result of lithium doping of D—C60 under different conditions, has the potential to be used in hydrogen storage studies due to both its high BET surface area and micropore volume.

In Fig. S.4 (Supplementary Material), the changes between hydrogen storage amount and BET surface area and hydrogen storage amount and micropore volume for C60, D—C60 and lithium doped defective fullerene samples at excess adsorption pressure at cryogenic temperature are presented. According to Pearson statistical analysis, the correlation coefficient between hydrogen storage amount and BET surface area was found to be 0.9033 and the correlation coefficient with micropore volume was found to be 0.8867. Since both of these coefficients are above 0.8, it is understood that both variables show a strong and positive relationship with hydrogen storage capacity. However, since the correlation coefficient with BET surface area is higher, it can be concluded that hydrogen storage capacity depends slightly more on BET surface area than micropore volume. BET surface area represents the total adsorption surface of the material and larger surface area means more places where hydrogen molecules can adhere to the surface. This directly increases the hydrogen storage capacity. Micropore volume, on the other hand, refers to the volume of porous structures where hydrogen will be physically trapped. This parameter is also important, but since micropores only allow molecules of certain sizes to be trapped, they may not provide as comprehensive an effect as surface area. In addition, some micropores being too narrow may make it difficult for hydrogen to access. As a result, although hydrogen storage capacity is affected by both factors, statistically, BET surface area stands out as a more decisive factor. Pearson correlation analyses revealed that the hydrogen storage capacity is strongly correlated with both BET surface area and micropore volume, showing an even higher degree of agreement with the BET surface area. This finding indicates that the positive effect obtained through the increase in surface area by Li doping is shaped by concurrent changes in structural agglomeration and pore accessibility.

Table 4 shows the hydrogen storage capacities of different carbon derivatives at different temperatures and pressures. Overall, the data indicate that higher storage capacities are generally achieved under low-temperature and high-pressure conditions. For example, D-C60–1 h-500 rpm (77 K, 100 bar, 2.17 wt%) has the highest capacity [15], which is substantially higher than the value found for C60 (77 K, 100 bar, 1.5 wt %). Notably, lithium doping of defective fullerene also improves performance, and Li-D-C60–01 M-200C-12 h reaches 1.9 wt% at 77 K and 100 bar. The beneficial role of metal incorporation is further supported by Pd—C60 (298 K, 300 bar, 0.85 wt%) and Ru—C60 (298 K, 300 bar, 0.69 wt%) [46]. When graphene-based materials are examined, Li-doped graphene (77 K, 20 bar, 1.416 wt%) has a higher capacity compared to pure graphene (0.607 wt%) [19]. Similarly, SWCNT (77 K, 20 bar, 1.605 wt%) and MWCNT (77 K, 20 bar, 1.42 wt%) offer a better storage capacity than graphene-based materials [19]. Importantly, hydrogen storage of SWCNT at higher temperature has also been reported (253 K, 60 bar, 0.9 wt%) [47], indicating that the temperature dependence can differ across carbon morphologies. However, in some cases lithium incorporation can be detrimental, as lithium doping decreased the hydrogen storage capacity for SWCNT (0.573 wt%) and MWCNT (0.53 wt%). By contrast, alternative alkali/metal strategies may remain highly effective at near-ambient conditions; for instance, K-doped MWCNT (313 K, 1 bar, 1.8 wt%) is remarkable for offering a very good capacity even at higher temperatures [48]. Moreover, transition-metal-doped CNTs such as Co-doped MWCNT (298 K, 21 bar, 1.06 wt %) and Li-doped MWCNT (298 K, 21 bar, 1.33 wt%) [49] demonstrate that appropriate metal incorporation and doping chemistry can significantly improve hydrogen adsorption even at near-ambient temperatures. In addition, functionalized carbon derivatives such as MWCNT-COOH (77 K, 80 bar, 1.17 wt%) and carbon spheres (77 K, 30 bar, 1.1 wt%) also have high hydrogen storage capacity [8,50], indicating that hydrogen storage performances of carbon-based materials can be improved by surface modifications. It should be emphasized that, although the hydrogen storage enhancement obtained in this study is moderate relative to some theoretical predictions, the fully experimental nature of the present system increases its practical relevance. Unlike many theoretical 2D fullerene systems that require idealized structures, the Li-doped defective fullerene materials synthesized here are experimentally accessible, parameter-tunable (concentration/temperature/time), and scalable, making the observed performance gains valuable for

Table 4
The comparison of hydrogen storage capacities of some carbon derivatives.

Samples	Temperatures (K)	Pressures (bar)	wt% H_2	References
Fullerene (D-C60–1 h-500 rpm)	77	100	2.17	[15]
C60	298	300	0.3	[46]
C70	77	20	0.045	[19]
Li-doped C70	77	20	0.53	[19]
Pd-C60	298	300	0.85	[46]
Ru-C60	298	300	0.69	[46]
C60	77	100	1.5	In this study
Li-D-C60–01 M-200C-12 h	77	100	1.9	In this study
Graphene	77	20	0.607	[19]
Li-doped graphene	77	20	1.416	[19]
SWCNT	77	20	1.605	[19]
Li-doped SWCNT	77	20	0.573	[19]
MWCNT	77	20	1.42	[19]
Li-doped MWCNT	77	20	0.53	[19]
K-doped MWCNT	313	1	1.8	[48]
MWCNT	77	10	0.28	[51]
Carbon sphere	77	30	1.1	[8]
MWCNT-COOH	77	80	1.17	[50]
Schiff base based MWCNT	77	10	0.37	[51]
SWCNT	253	60	0.9	[47]
Co-doped MWCNT	298	21	1.06	[49]
Li-doped MWCNT	298	21	1.33	[49]

adsorption-based hydrogen storage design.

3.4. Adsorption isotherms

An adsorption isotherm describes the relationship between the amount of gas adsorbed and its equilibrium pressure at constant temperature, and it is a fundamental tool for understanding adsorption mechanisms. The adsorption behavior is commonly described using Freundlich, Langmuir, Dual-Langmuir, and Temkin models [52]. The linearized form of the Freundlich isotherm can be expressed as follows:

$$lnq_e = lnk_F + 1/nlnP \quad (1)$$

where q_e is the amount of adsorbate adsorbed at equilibrium (mmol/g), k_F and n are Freundlich model constants, and P is the equilibrium pressure (bar) [54].

The Langmuir isotherm model, which assumes monolayer adsorption on a homogeneous surface, can be written in linear form as [54]:

$$\frac{P}{q_e} = \frac{1}{K_1 q_{m1}} + \frac{P}{q_{m1}} \quad (2)$$

where q_{m1} is the monolayer adsorption capacity (mmol/g) and K_1 is the Langmuir equilibrium constant. From the slope and intercept of the P/q_e versus P plot, the Langmuir parameters q_{m1} and K_1 can be determined.

Similarly, the Dual-Langmuir model, which assumes two distinct adsorption sites and dissociative adsorption of hydrogen molecules, is expressed as:

$$\frac{P^{1/2}}{q_e} = \frac{1}{K_2 q_{m2}} + \frac{P^{1/2}}{q_{m2}} \quad (3)$$

In this equation, q_{m2} and K_2 are numerical values, which are different from those in eq. 2 [52].

The Temkin adsorption isotherm assumes that the surface is not homogeneous and that the adsorption energy increases linearly with the fraction of the surface covered. The linear form of the equation is:

$$q_e = AlnP + B \quad (4)$$

In this equation, A and B are specific constants related to the Temkin model [52,55].

Table 5 summarizes the isotherm constants and regression coefficients obtained by fitting the experimental hydrogen adsorption data to the Freundlich, Langmuir, Dual-Langmuir, and Temkin models. The regression coefficients for the Freundlich, Langmuir, Dual-Langmuir, and Temkin models were found to be 0.9571–0.9983, 0.8212–0.9959, 0.5897–0.9919, and 0.7195–0.9983, respectively. Overall, the Freundlich and Langmuir models exhibited the highest correlation coefficients, indicating their strong applicability to the present adsorption system. The Freundlich parameter n was found to vary between 1.46 and 3.92. Values of $n > 1$ indicate favorable adsorption and suggest that adsorption occurs on relatively homogeneous and energetically stable surfaces, whereas $n < 1$ generally corresponds to heterogeneous surfaces or multilayer adsorption processes. For the Langmuir model, the calculated monolayer capacities were in good agreement with the experimental q_e values, indicating that hydrogen adsorption on Li-doped defective fullerenes predominantly follows monolayer adsorption on energetically uniform sites. This suggests that the adsorption surface exhibits homogeneous. In the literature, hydrogen adsorption on porous adsorbents has been reported to fit both Freundlich and Langmuir-type models depending on surface heterogeneity and pore structure. For instance, hydrogen adsorption on porous materials was reported to follow the Freundlich model, indicating preferential adsorption on heterogeneous surfaces and the significant role of micropores in hydrogen storage capacity [56].

Hydrogen adsorption on boron-doped carbon nanotubes (BCNTs) showed better agreement with the Langmuir model, with storage capacities of 0.157 wt% at 303 K and 2.5 wt% at 77 K [57]. Furthermore, adsorption data on granular activated carbon were better explained by the Langmuir–Freundlich model, which accounts for surface heterogeneity and temperature-dependent adsorption behavior [58]. These findings collectively demonstrate that hydrogen adsorption behavior strongly depends on the surface chemistry, pore structure, and energetic heterogeneity of the adsorbent material.

3.5. Adsorption rate and kinetics

Adsorption is a multistep process involving the transport of adsorbate molecules from the bulk phase to the external surface of the adsorbent, followed by diffusion into internal pores and subsequent surface adsorption. The adsorption mechanism strongly depends on environmental conditions, surface chemistry, pore structure, and adsorbate–adsorbent interactions. Because each adsorbent possesses distinct active sites and pore architectures, the rate-determining step of adsorption may vary among different systems [59,60]. Fig. S.5 (Supplementary Material) presents the time-dependent hydrogen storage capacities of fullerene-based samples at different pressures. The storage capacities and adsorption rates increase with increasing pressure. This behavior can be attributed to the increase in hydrogen gas density and enhanced van der Waals interactions at higher pressures, which promote stronger interactions between hydrogen molecules and the adsorbent surface. As a result, a greater number of hydrogen molecules interact with available adsorption sites per unit time, leading to an increase in the adsorption rate. The adsorption kinetics exhibit a typical two-stage behavior. Initially, the adsorption rate increases rapidly, followed by a gradual slowdown, and eventually reaches equilibrium. This rapid initial uptake is associated with the availability of abundant unoccupied active sites and low surface coverage. As adsorption progresses, the number of available active sites decreases, surface coverage increases, and diffusion resistance becomes significant, leading to a reduction in adsorption rate until equilibrium is achieved. It is also observed that the initial adsorption rate is higher at elevated pressures, reflecting the increased driving force for mass transfer. The adsorption rate data in Fig. S.5 provide insights into the adsorption mechanism, rate-

Table 5
Isotherm analysis results for experimental data.

Samples	q_{exp} (mmol/g)	Langmuir			Dual Langmuir R^2	Freundlich			Temkin R^2
		q_m (mmol/g)	K_1	R^2		n_F	k_F	R^2	
C60	0.19	0.27	0.048	0.8212	0.5897	1.46	0.016	0.9687	0.7195
D-C60	0.37	0.38	0.179	0.9617	0.7935	2.52	0.084	0.9983	0.8173
Li-D-C60–0001 M-200C-6 h	0.27	0.28	0.770	0.9936	0.9919	3.03	0.119	0.9588	0.9587
Li-D-C60–001 M-200C-6 h	0.32	0.33	0.640	0.9930	0.9871	3.07	0.132	0.9571	0.9502
Li-D-C60–01 M-200C-6 h	0.33	0.34	1.262	0.9959	0.9876	3.78	0.179	0.9774	0.9452
Li-D-C60–01 M-160C-6 h	0.21	0.21	0.856	0.9910	0.9729	3.70	0.103	0.9916	0.9361
Li-D-C60–01 M-240C-6 h	0.19	0.19	1.258	0.9949	0.9882	3.92	0.104	0.9822	0.9687
Li-D-C60–01 M-200C-2 h	0.20	0.20	1.027	0.9945	0.9866	3.77	0.102	0.9824	0.9616
Li-D-C60–01 M-200C-12 h	0.21	0.21	0.839	0.9910	0.9733	3.68	0.102	0.9933	0.9380

determining step, and the relative contributions of mass transfer, pore diffusion, and surface adsorption processes. In the literature, various kinetic models, including pseudo-first-order, pseudo-second-order, and Elovich models, have been widely applied to describe adsorption kinetics for gas and liquid-phase systems [15,19]. These models enable the quantitative evaluation of adsorption mechanisms and identification of diffusion-controlled or surface-reaction-controlled processes. The linear form of the pseudo-first-order kinetic model can be expressed as follows:

$$\ln(q_e - q_t) = lnq_e - k_1 t \quad (5)$$

In this equation, q_e is the amount of adsorbate adsorbed at equilibrium (mmol/g); q_t is the amount of adsorbate adsorbed at any time t (mmol/g); k_1 is the adsorption rate constant (min^{-1}); and t is time (min). In order for the experimental data to be compatible with this equation, the plot of $ln(q_e\text{-}q_t)$ against t should give a straight line. The k_1 and q_e values are calculated from the slope and extrapolation values of the line [61].

Linear pseudo second order kinetic equation

$$\frac{t}{q_t} = \frac{1}{k_2 q_e^2} + \frac{t}{q_e} \quad (6)$$

In this equation, q_e is the amount of adsorbate adsorbed at equilibrium (mmol/g); k_2 is the rate constant (g/mmol min); q_t is the amount of adsorbate adsorbed at any time t (mmol/g); and t is time (min). According to this equation, the curve of t/q_t against t should give a straight line. From the slope and extrapolation values, q_e and k_2 values can be calculated, respectively [62].

Another kinetic model is the Elovich equation. The Elovich equation is suitable for systems with heterogeneous surfaces in chemical adsorption processes. Its linear form can be written as follows:

$$q_t = \alpha lnt + \alpha ln(\alpha\beta) \quad (7)$$

In this equation, α is the initial adsorption rate and β is the desorption constant. If the experimental data fit this equation, the plot of q_t against lnt should give a straight line with slope, α, and extrapolation, $\alpha\ln(\alpha\beta)$. From the slope and extrapolation, α and β can be calculated [63].

The regression coefficient values and other kinetic constants obtained by applying the experimental data to the pseudo-first-order, pseudo-second-order, and Elovich equations are presented in Table 6. The regression coefficient (R^2) values for the pseudo-first-order model range from 0.3771 to 0.7365, whereas those for the pseudo-second-order model range from 0.9817 to 0.998, and for the Elovich model from 0.5918 to 0.9162. Among the tested models, the pseudo-second-order model exhibits the highest regression coefficients, indicating the best fit to the experimental data. Another parameter confirming the agreement between the experimental data and the pseudo-second-order model is the comparison between the experimental and calculated q_e values. Except for four samples, the calculated and experimental q_e values are in very good agreement, with deviations of approximately 5%. These results clearly demonstrate that the hydrogen adsorption kinetics are best described by the pseudo-second-order kinetic model. Fig. S.6 (Supplementary Material) shows the plots of t/q_t versus t for fullerene samples at different pressures. In addition, the fitting curves generated using the calculated q_e and k_2 values are presented in Fig. S.5 (Supplementary Material). A very good agreement between the experimental data and the fitted curves is observed, further validating the applicability of the pseudo-second-order model. A similar kinetic behavior was reported for hydrogen adsorption on defective fullerene surfaces produced by high-energy tungsten carbide mortar ball milling, where pseudo-first-order and pseudo-second-order models were applied and the regression coefficients for the pseudo-second-order model ranged between 0.87 and 0.99 [15]. Likewise, the adsorption kinetics of benzene vapor on almond-shell-derived char were found to follow the pseudo-second-order kinetic mode [64]. In another study, the adsorption kinetics of hydrogen gas on Pt/TiO_2/Pt-based sensors were investigated, and the experimental data showed excellent agreement with Ho's pseudo-second-order model, with correlation coefficients higher than 0.99 [65]. Furthermore, the adsorption kinetics of NO_2 on hydrothermally synthesized SnO_2/RGO nanohybrids were described by the Elovich model at low concentrations and by the pseudo-second-order model at higher concentrations, highlighting the concentration-dependent adsorption mechanism [66].

3.6. Adsorption mechanism

The determination of the rate-limiting step plays a key role in understanding the adsorption mechanism. In general, the adsorption process consists of three consecutive steps: (i) diffusion of the adsorbate from the bulk phase to the external surface of the adsorbent, (ii) intraparticle diffusion of the adsorbate into the internal pores, and (iii) adsorption at the active sites on the adsorbent surface. The slowest of these steps governs the overall adsorption rate and can be identified by applying kinetic models such as the Boyd, Avrami, and Weber–Morris equations.

The linear Boyd equation for the external mass transfer of adsorbate from the bulk phase to the adsorbent surface can be given as follows.

$$ln\left(1 - \frac{q_t}{q_e}\right) = -0.497 - \frac{\pi^2 D_c}{r_c^2} t \quad (8)$$

In this equation, D_c is the diffusion coefficient (cm^2/min); r_c is the diameter of the adsorbent (cm); t is the time (min); q_t is the amount of substance adsorbed at any time t (mmol/g); and q_e is the amount of adsorbate adsorbed at equilibrium (mmol/g). According to the equation above, if the curve of $ln(1\text{-}q_t/q_e)$ against t intersects the y-axis at −0.497, it can be said that the adsorption mechanism is external mass transfer. If it gives a straight line passing through the origin, the adsorption mechanism is intraparticle diffusion. If the diameter of the particles is known, D_c can be calculated from the slope of the graph [59].

The Avrami equation is another model used to elucidate the possible changes in the adsorption mechanism that occur during the adsorption process. Its linear form is

$$ln[-ln(1-\theta)] = lnk + nlnt \quad (9)$$

In this equation, θ is the coverage fraction (q_t/q_e); k is the kinetic constant; and n is a constant related to the adsorption mechanism. According to this equation, the plot of $ln[-ln(1\text{-}\theta)]$ against lnt gives a straight line with slope n and extrapolation lnk. If the Avrami equation gives a straight line passing through the origin and/or the value of n is less than one, it can be said that the adsorption mechanism is diffusion controlled. n and k can be calculated from the slope and extrapolation values [67].

The Weber-Morris equation developed to describe intraparticle diffusion can be written in linear form as follows:

$$q_t = k_{int}\sqrt{t} + C \quad (10)$$

In this equation, k_{int} is the intraparticle diffusion rate constant and C is a constant representing the intraparticle diffusion effect. The values of C and k_{int} can be found from the extrapolation and slope values of the curve of q_t versus $t^{0.5}$. If the curve passes through the origin, the rate determining step is intraparticle diffusion. Sometimes it can be obtained from two or three intersecting lines with different slopes [68,69].

In order to elucidate the adsorption mechanism, linear regression coefficient values were calculated for the relevant kinetic equations. The data in Table 6 show that the regression coefficient values for the Boyd equation ranged from 0.1515 to 0.6082 and for the Avrami equation ranged from 0.5102 to 0.8899. Another parameter that provides information about the adsorption mechanism for the Avrami equation is the n value. It is seen from the table that the n value is less than one. Although the regression coefficient for the Avrami equation is low, the n value indicates that hydrogen adsorption on fullerene surfaces may be

Table 6
Calculated kinetic constants for hydrogen adsorption on the surface of fullerene samples at different pressures.

Samples	Pressure (bar)	First order	Second order				Elovich	Boyd	Weber-Morris						Avrami		
		R^2	R^2	$q_{e(exp)}$	$q_{e(cal)}$	k_2	R^2	R^2	R_1^2	k_1	R_2^2	k_2	R_3^2	k_3	R^2	n	K_{Av}
C60	42	0.6877	0.9906	0.808	0.783	4.63	0.9162	0.6082	0.9290	0.913	0.9145	0.471	0.3282	0.088	0.8899	0.51	1.31
	35	0.6405	0.9902	0.655	0.591	9.20	0.8786	0.5331	0.9510	0.907	0.6557	0.189	0.2484	0.057	0.8582	0.41	1.32
	27	0.5249	0.9817	0.416	0.361	15.02	0.7844	0.5279	0.9389	0.515	0.5805	0.116	0.0646	0.028	0.7986	0.35	1.25
D-C60	42	0.4340	0.9926	0.994	0.928	13.13	0.7901	0.3736	0.9905	1.552	0.6903	0.362	0.0001	0.001	0.7367	0.35	1.77
	35	0.6892	0.9887	0.660	0.634	7.38	0.8689	0.5802	0.9830	1.002	0.4461	0.161	0.3828	0.080	0.7833	0.37	1.50
	27	0,4701	0,9874	0.443	0.382	19.76	0.7982	0.4390	0.9330	0.523	0.6640	0.147	0.013	0.011	0.8225	0.38	1.33
Li-D-C60–0001 M-200-6 h	42	0.6859	0.9960	1.030	1.004	5.96	0.8829	0.5028	0.9715	1.185	0.5819	0.163	0.2273	0.094	0.8442	0.42	1.67
	35	0.6580	0.9929	0.662	0.629	9.31	0.8784	0.5173	0.9329	0.780	0.6067	0.136	0.0714	0.046	0.8371	0.40	1.56
	27	0.3750	0.9854	0.398	0.361	24.31	0.7664	0.3936	0.8930	0.452	0.6345	0.093	0.0118	0.018	0.7396	0.45	1.55
Li-D-C60–001 M-200-6 h	42	0.6514	0.9959	0.976	0.930	7.66	0.8904	0.4886	0.9240	0.957	0.7800	0.246	0.1610	0.067	0.8496	0.40	1.62
	35	0.6249	0.9919	0.651	0.612	10.59	0.8713	0.5010	0.9353	0.674	0.4996	0.097	0.0255	0.028	0.8637	0.41	1.58
	27	0.6476	0.9902	0.458	0.427	12.80	0.8614	0.5434	0.9456	0.518	0.6364	0.106	0.0021	0.006	0.8317	0.42	1.46
Li-D-C60–01 M-200-6 h	42	0.5966	0.9969	1.021	0.953	9.38	0.8608	0.4392	0.9576	1.032	0.5989	0.161	0.0174	0.020	0.8414	0.37	1.63
	35	0.6055	0.9933	0.687	0.636	11.95	0.8631	0.4712	0.9648	0.900	0.8340	0.198	0.0619	0.033	0.7807	0.36	1.54
	27	0.5281	0.9867	0.462	0.401	15.68	0.7782	0.4899	0.9484	0.640	0.7699	0.161	0.0672	0.029	0.7174	0.31	1.32
Li-D-C60–01 M-160-6 h	42	0.6242	0.9995	4.705	4.636	4.65	0.7107	0.2594	0.9914	9.831	0.7698	0.681	0.2804	0.139	0.6446	0.30	2.58
	35	0.6909	0.9995	3.495	3.474	5.14	0.7319	0.2811	0.9806	7.144	0.7231	0.450	0.5485	0.160	0.8109	0.31	2.72
	27	0.5737	0.9986	2.361	2.271	8.38	0.7110	0.2666	0.9596	4.710	0.6757	0.250	0.2658	0.097	0.6948	0.22	2.33
Li-D-C60–01 M-240-6 h	42	0.7061	0.9992	4.145	4.085	4.04	0.7770	0.3053	0.9591	8.443	0.8009	0.673	0.4667	0.203	0.8519	0.28	2.56
	35	0.4984	0.9990	3.212	3.136	6.82	0.7744	0.2933	0.9623	6.288	0.8754	0.641	0.1761	0.095	0.7490	0.28	2.52
	27	0.4372	0.9979	2.224	2.123	9.73	0.6578	0.2365	0.9466	4.378	0.5164	0.234	0.1742	0.093	0.6137	0.19	2.32
Li-D-C60–01 M-200-2 h	42	0.4676	0.9992	5.378	5.279	4.07	0.7599	0.2881	0.9849	10.938	0.8285	0.942	0.1030	0.107	0.7815	0.31	2.59
	35	0.5195	0.9992	3.966	3.843	6.63	0.6653	0.2285	0.9824	8.008	0.6323	0.419	0.1554	0.088	0.7532	0.24	2.52
	27	0.3771	0.9991	2.807	2.724	14.97	0.5918	0.1761	0.9705	6.063	0.5880	0.299	0.0808	0.048	0.6432	0.21	2.75
Li-D-C60–01 M-200-12 h	42	0.7365	0.9998	8.063	8.038	2.976	0.7448	0.2456	0.9450	16.929	0.8622	1.067	0.6003	0.253	0.8318	0.29	3.02
	35	0.4151	0.9997	6.249	6.165	8.769	0.6690	0.1798	0.9146	12.636	0.8635	0.728	0.0001	0.001	0.6469	0.24	3.18
	27	0.4357	0.9993	4.527	4.407	10.50	0.5991	0.1515	0.9414	11.276	0.7113	0.384	0.0889	0.067	0.5102	0.18	2.88

diffusion controlled. According to the Weber-Morris equation, in order for the only rate-determining step to be intraparticle diffusion, the curve of q_t versus $t^{0.5}$ should give a straight line passing through the origin. However, as can be seen from Fig. 10, it is seen that three intersecting lines with different slopes are obtained. The regression coefficient of the first curve is in the range of 0.8930–0.9914, the regression coefficient of the second curve is in the range of 0.4461–0.9145, and the regression coefficient of the third curve is quite low. Since the regression coefficient of the first curve is higher than that of the Boyd and Avrami equations and the other two curves and passes through the origin and/or a point very close to the origin, it can be said that the step controlling the reaction rate is intraparticle diffusion. Another experimental result supporting this case is the adsorption rate curves in Fig. S.5 (Supplementary Material). When the curves are examined, it is seen that the adsorption reaches equilibrium in about one minute. For the points up to the first minute, it is seen that the q_t versus $t^{0.5}$ curve will pass through the origin or a point very close to the origin. These results support that the adsorption mechanism occurs by intraparticle diffusion in the pores. The adsorption mechanism of CO_2 on the polyaspartamide surface was investigated using a series of diffusion models. The research revealed that intraparticle diffusion is the main source of resistance in the movement of gas molecules onto polyaspartamide. While film diffusion was determined as the dominant mechanism at the beginning of the adsorption process, this mechanism loses its effect over time as it approaches equilibrium. As a result, it was determined that both film and intraparticle diffusion play important roles in the adsorption mechanism of CO_2 on polyaspartamide [70]. In another study, the adsorption mechanism of CO_2 and H_2 gases on HDPE membranes was investigated under different temperature and pressure conditions. The adsorption process was described in three stages: first, gas molecules diffused to the outer surface of the membrane; then, gas molecules migrated from the liquid phase near the surface of the membrane; finally, gas molecules dissolved in the polymer chains and were adsorbed. At low temperatures, it was observed that the adsorption obeyed the pseudo-second-order kinetic model, while at high temperatures, the intraparticle diffusion mechanism was dominant. These findings indicate that increasing the temperature reduces the adsorption capacity and that HDPE membranes can be used more effectively in gas separation applications at low temperatures [71]. The adsorption of methane gas on activated carbon produced from palm kernel shell was found to be consistent with the pseudo-first-order kinetic model. The intraparticle diffusion model revealed that methane adsorption was affected by both pore diffusion and outer layer diffusion. These studies, similar to our results, show that the adsorption mechanism of different gases on solid surfaces is based on intraparticle diffusion [72].

In the light of the above explanations, the adsorption mechanism of hydrogen on the surfaces and interiors of C60, D—C60 and Li-D-C60–01 M-200C-12 h samples can be shown as in Fig. 11. In fullerene, hydrogen can be stored on the outer surfaces of fullerene molecules and between fullerene molecules; in D—C60, in the interiors of defective fullerenes, on their exterior surfaces and between defective fullerenes; and in Li-D-C60–01 M-200C-12 h, on the outer surface of defective fullerene, between defective fullerenes, in the interiors of defective fullerenes, around lithium atoms in the interiors of defective fullerenes and around lithium atoms bonded to hydroxyl groups on the surface of defective fullerene. Compared with recently reported two-dimensional fullerene networks, which exhibit extremely high theoretical hydrogen storage capacities due to combined chemisorption and physisorption mechanisms, the Li-doped defective fullerene system investigated in this study offers a more experimentally feasible and structurally simpler platform. While 2D fullerene lattices provide extraordinary theoretical storage capacities, their synthesis and practical implementation remain challenging. In contrast, Li doping in defective fullerene introduces a controllable hydrogen adsorption and release mechanism, where Li

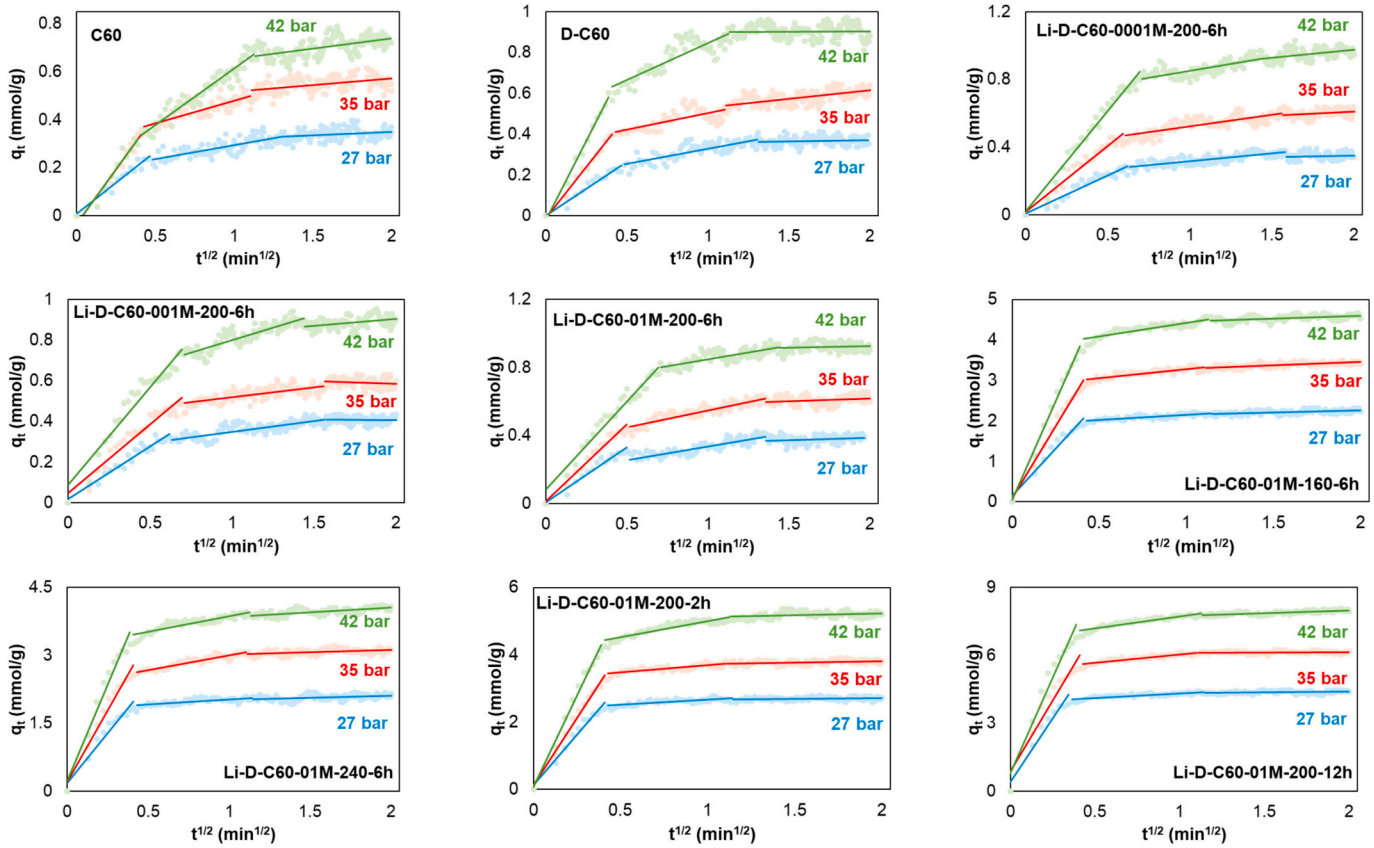

Fig. 10. The curves of q_t versus $t^{0.5}$ for fullerene samples at different pressures.

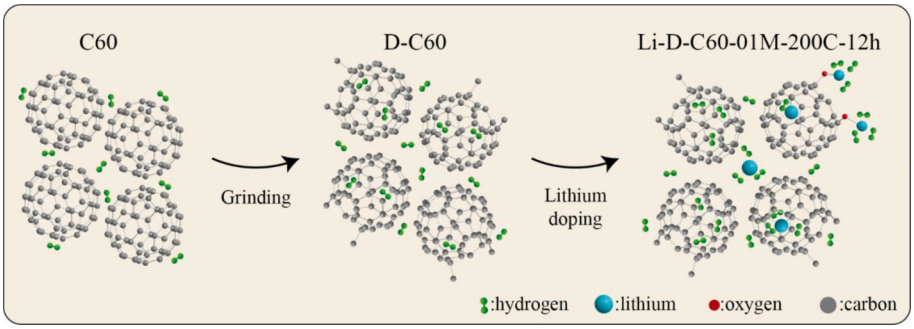

Fig. 11. Adsorption mechanism of hydrogen at C60, D—C60 and Li-D-C60–01 M-200C-12 h.

atoms act as hydrogen release valves, enhancing safety and reversibility. Therefore, although the storage enhancement is moderate, the Li-doped defective fullerene system presents a realistic and promising candidate for practical hydrogen storage applications [16]. This behavior is consistent with the adsorption–desorption pathways illustrated in Fig. 11, where Li atoms act as reversible hydrogen binding and release centers within the defective fullerene framework.

3.7. Conclusions

In this study, the production, characterization, hydrogen storage capacities, isotherm and kinetic analyses of defective and lithium-doped defective fullerenes were comprehensively investigated. Compared to C60, the BET surface area of D—C60 increased by 274%, reaching 168.9 m^2/g. DTA/TG analysis revealed that the thermal stability of both D—C60 and Li-doped defective fullerenes decreased, likely due to increased structural defects and the presence of impurities, especially moisture. According to thermal decomposition profiles, C60 decomposed in a single step, D—C60 in two steps, and Li-doped defective fullerenes in three steps. Morphological characterizations demonstrated significant alterations in shape and particle size distribution after the defect formation process. Hydrogen storage capacities of all samples were significantly higher at cryogenic temperature. At room temperature, hydrogen storage increased linearly with pressure, whereas at cryogenic conditions, the capacity initially increased rapidly, reached a maximum, then slightly decreased, and finally increased again with further pressure rise. This behavior is characteristic of excess adsorption under cryogenic conditions. Among the tested samples, Li-D-C60–01 M-200C-12 h exhibited the highest hydrogen storage capacity, while D—C60 showed a 191% increase at cryogenic temperature compared to C60. EIS analyses revealed that lithium doping under optimized conditions (0.1 M, 200 °C, 6 h) significantly reduced the impedance compared to both C60 and D—C60, indicating enhanced electrical conductivity due to increased charge carrier mobility and improved interfacial properties and moreover, that the electrochemical behavior of the materials is predominantly governed by a diffusion-controlled reaction mechanism, indicating that ion transport within the porous structure plays a critical role in the overall conductivity performance. In parallel, Pearson correlation analysis demonstrated strong relationships between hydrogen storage capacity and key structural parameters, particularly BET surface area ($r = 0.9033$) and micropore volume ($r = 0.8867$), confirming the critical role of textural and electronic factors in adsorption performance. Pearson correlation analyses showed that the hydrogen storage capacity exhibits a strong positive correlation with both BET surface area and micropore volume, with the highest correlation found for BET surface area. These results indicate that the effect of Li doping is governed not only by the increase in surface area but also by Li-induced structural rearrangements that alter pore accessibility and agglomeration behavior. The near-unity regression coefficients obtained for the Langmuir model further confirm monolayer physisorption on energetically homogeneous adsorption sites. Kinetic analyses showed that hydrogen gas adsorption was initially rapid, gradually slowed with time, and eventually reached equilibrium. The pseudo-second-order kinetic model provided the best fit to experimental data, with regression coefficients ranging from 0.9817 to 0.998. Furthermore, application of the Weber–Morris model indicated that intraparticle diffusion was the rate-determining step. Importantly, Li centers in the defective fullerene framework can act as controllable hydrogen release valves, enabling safer and more reversible hydrogen desorption compared to pristine fullerene systems. These findings collectively highlight that the adsorption mechanism is governed by a combination of surface functionality, diffusion kinetics, and pore accessibility, all of which are tunable through lithium doping strategies.

CRediT authorship contribution statement

Yasemin Turhan: Writing – original draft, Supervision, Software, Methodology, Investigation, Formal analysis, Data curation. **Betül Duman:** Methodology, Investigation. **Mehmet Doğan:** Writing – review & editing, Writing – original draft, Visualization, Validation, Supervision, Software, Resources, Project administration, Methodology, Investigation, Funding acquisition, Formal analysis, Data curation, Conceptualization. **Ersin Yanmaz:** Software, Methodology, Investigation, Data curation. **Zeynep Bicil:** Writing – original draft, Software, Methodology, Investigation, Formal analysis, Data curation. **Berna Koçer Kızılduman:** Writing – original draft, Validation, Software, Methodology, Investigation, Formal analysis, Data curation.

Declaration of competing interest

The authors declare that they have no known competing financial interests or personal relationships that could have appeared to influence the work reported in this paper.

Acknowledgments

This work was supported by TUBİTAK (Project Number: 123Z536).

Appendix A. Supplementary data

Supplementary data to this article can be found online at https://doi.org/10.1016/j.diamond.2026.113399.

Data availability

Data will be made available on request.

References

[1] E.E. Doğan, Hydrogen production and its storage from solar energy, Adv. Mater. Sci. 20 (2020) 14–25, https://doi.org/10.2478/adms-2020-0007.

[2] K. Isinkaralar, G. Gullu, A. Turkyilmaz, M. Dogan, O. Turhan, Activated carbon production from horse chestnut shells for hydrogen storage, Int. J. Glob. Warm. 26 (2022) 361–373, https://doi.org/10.1504/IJGW.2022.122430.

[3] A.S. Mekonnin, K. Wacławiak, M. Humayun, S. Zhang, H. Ullah, Hydrogen storage technology, and its challenges: a review, Catalysts 15 (2025) 260, https://doi.org/10.3390/catal15030260.

[4] Y. Wen, X. Chai, Y. Gu, W. Wu, W. Ma, J. Zhang, T. Zhang, Advances in hydrogen storage materials for physical H_2 adsorption, Int. J. Hydrog. Energy 97 (2025) 1261–1274, https://doi.org/10.1016/j.ijhydene.2024.11.459.

[5] L. Wang, R.T. Yang, New sorbents for hydrogen storage by hydrogen spillover – a review, Energy Environ. Sci. 1 (2008) 268–279, https://doi.org/10.1039/B807957A.

[6] A.I. Osman, W. Abd-Elaziem, M. Nasr, Enhanced hydrogen storage efficiency with sorbents and machine learning: a review, Environ. Chem. Lett. 22 (2024) 1703–1740, https://doi.org/10.1007/s10311-024-01741-3.

[7] V. Soni, S. Sonu, P. Singh, S. Thakur, T. Ahamad, V.-H. Nguyen, V. Chaudhary, N. Kumar, S. Kaya, C.M. Hussain, P. Raizada, Oxygen vacancy enriched $SrTiO_3$ and NiO-based S-scheme heterojunction moored on activated carbon from exhausted water filter batteries for ameliorated photodegradation of doxycycline hydrochloride and methyl orange degradation, J. Taiwan Inst. Chem. Eng. 159 (2024) 105419, https://doi.org/10.1016/j.jtice.2024.105419.

[8] B.K. Kızılduman, Y. Turhan, M. Doğan, Mesoporous carbon spheres produced by hydrothermal carbonization from rice husk: optimization, characterization and hydrogen storage, Adv. Powder Technol. 32 (2021) 4222–4234, https://doi.org/10.1209/0295-5075/96/27013.

[9] H. Jindal, A.S. Oberoi, I.S. Sandhu, M. Chitkara, B. Singh, Graphene for hydrogen energy storage – a comparative study on GO and rGO employed in a modified reversible PEM fuel cell, Int. J. Energy Res. 45 (2021) 5815–5826, https://doi.org/10.1002/er.6202.

[10] R. Mohan, R. Paulose, Influence of ferrites nanoparticles anchored on CNT hybrid nanocomposites for high-performance energy storage applications, J. Electron. Mater. 47 (2018) 6878–6885, https://doi.org/10.1007/s11664-018-6615-9.

[11] O.V. Pupysheva, A.A. Farajian, B.I. Yakobson, Fullerene nanocage capacity for hydrogen storage, Nano Lett. 8 (2008) 767–774, https://doi.org/10.1021/nl071436g.

[12] W. Dai, M. Xiao, M.-Q. Chen, J.-J. Xu, Y.-J. Tang, A simulation study on the hydrogen storage properties of fullerene family molecules C_x (x = 56, 60, 70) and their hydrides, Mod. Phys. Lett. B 30 (2016) 1650303, https://doi.org/10.1142/S0217984916503036.

[13] M. Gaboardi, N. Sarzi Amadè, M. Aramini, C. Milanese, G. Magnani, S. Sanna, M. Riccò, D. Pontiroli, Extending the hydrogen storage limit in fullerene, Carbon 120 (2017) 77–82, https://doi.org/10.1016/j.carbon.2017.05.025.

[14] J.A. Teprovich Jr., D.A. Knight, B. Peters, R. Zidan, Comparative study of reversible hydrogen storage in alkali-doped fulleranes, J. Alloys Compd. 580 (2013) S364–S367, https://doi.org/10.1016/j.jallcom.2013.02.024.

[15] M. Doğan, M.Y. Kalafat, B.K. Kızılduman, Z. Bicil, Y. Turhan, E. Yanmaz, B. Duman, Hydrogen storage analysis of fullerene and defective fullerenes: the first experimental study, Fuel 390 (2025) 134705, https://doi.org/10.1016/j.fuel.2025.134705.

[16] Y. Ren, Y. Lu, D. Zhang, Enhanced hydrogen storage capacity in two-dimensional fullerene networks, J. Phys. Chem. Lett. 14 (2023) 11051–11057, https://doi.org/10.1021/acs.jpclett.3c02488.

[17] F.N. Yalçınkaya, M. Doğan, Z. Bicil, B.K. Kizilduman, Effect of functionalization and Li-doping methods to hydrogen storage capacities of MWCNTs, Fuel 372 (2024) 132274, https://doi.org/10.1016/j.fuel.2024.132274.

[18] M. Doğan, Z. Bicil, B.K. Kızılduman, Y. Turhan, F. Pehlivan, Functionalization and metal doping of MWCNTs for hydrogen storage, J. Energy Storage 122 (2025) 116653, https://doi.org/10.1016/j.est.2025.116653.

[19] Z.S. Doğan, E.E. Doğan, Z. Bicil, B.K. Kızılduman, The effect of Li-doping and doping methods to hydrogen storage capacities of some carbonaceous materials, Fuel 396 (2025) 135820, https://doi.org/10.1016/j.fuel.2025.135280.

[20] A. Gromov, D. Ostrovskii, A. Lassesson, M. Jönsson, E.E.B. Campbell, Fourier transform infrared and Raman spectroscopic study of chromatographically isolated Li@C_{60} and Li@C_{70}, J. Phys. Chem. B 107 (2003) 11290–11301, https://doi.org/10.1021/jp030403w.

[21] M. Anafcheh, Li-decorated fullerenes: a DFT study, J. Clust. Sci. 30 (2019) 69–76, https://doi.org/10.1007/S10876-018-1465-4.

[22] A.J. Khan, M. Hanif, M.S. Javed, Synthesis, characterization and charge storage properties of C60-fullerene microparticles as a flexible negative electrode for supercapacitors, J. Mater. Sci. Mater. Electron. 30 (2019) 8568–8576, https://doi.org/10.1007/s10854-019-01177-4.

[23] B.M. Ginzburg, S. Tuichiev, S.K. Tabarov, A.A. Shepelevskii, L.A. Shibaev, X-ray diffraction analysis of C_{60} fullerene powder and fullerene soot, Tech. Phys. 50 (2005) 1458–1461, https://doi.org/10.1134/1.2131953.

[24] W. Zhu, D.E. Miser, W.G. Chan, M.R. Hajaligol, Characterization of combustion fullerene soot, C_{60}, and mixed fullerene, Carbon 42 (2004) 1463–1471, https://doi.org/10.1016/j.carbon.2004.01.076.

[25] T. Itoh, S. Nitta, S. Nonomura, X-ray diffraction patterns of C_{60} films by the thin film method and the intercalation of O_2, Appl. Surf. Sci. 113 (1997) 282–285, https://doi.org/10.1016/S0169-4332(96)00951-8.

[26] H. Qian, X. Li, Q. Chen, W. Liu, Z. Zhao, Z. Ma, Y. Cao, J. Wang, W. Li, K. Xu, K. Zhang, W. Yan, J. Zhang, X. Li, LiZn/Li_2O induced chemical confinement enabling dendrite-free Li-metal anode, Adv. Funct. Mater. 34 (2024) 2310143, https://doi.org/10.1002/adfm.202310143.

[27] F. Cataldo, A study on the thermal stability to 1000 °C of various carbon allotropes and carbonaceous matter both under nitrogen and in air, Fullerenes Nanotubes Carbon Nanostruct. 10 (2002) 293–311, https://doi.org/10.1081/FST-120016451.

[28] W. Zhu, D.E. Miser, W.G. Chan, M.R. Hajaligol, Characterization of combustion fullerene soot, C_{60}, and mixed fullerene, Carbon 42 (2004) 1463–1471, https://doi.org/10.1016/j.carbon.2004.01.076.

[29] V. Oleshko, E. Fastow, K. Scott, J. Cumings, Experimental evaluation of lithium detection limits by windowless SDD EDXS and EELS in a binary Al–Li alloy powder, Microsc. Microanal. 26 (2020) 986–987.

[30] Y. Yuan, K. Yu, C. Zhang, X. Liu, Generation of textured surfaces by vibration-assisted ball-end milling, Nanomanuf. Metrol. 6 (2023) 19, https://doi.org/10.1007/s41871-023-00198-2.

[31] J. Brant, H. Lecoanet, M.R. Wiesner, Aggregation and deposition characteristics of fullerene nanoparticles in aqueous systems, J. Nanopart. Res. 7 (2005) 545–553, https://doi.org/10.1007/s11051-005-4884-8.

[32] K.L. Chen, M. Elimelech, Aggregation and deposition kinetics of fullerene (C_{60}) nanoparticles, Langmuir 22 (2006) 10994–11001, https://doi.org/10.1021/la062072v.

[33] U. Ritter, Y.I. Prylutskyy, M.P. Evstigneev, N.A. Davidenko, V.V. Cherepanov, A. I. Senenko, A.G. Naumovets, Structural features of highly stable reproducible C_{60} fullerene aqueous colloid solution probed by various techniques, Fullerenes Nanotubes Carbon Nanostruct. 23 (2015) 530–534, https://doi.org/10.1080/1536383X.2013.870900.

[34] A.J. Bard, L.R. Faulkner, Electrochemical Methods: Fundamentals and Applications, second ed., Wiley, New York, 2001.

[35] A. Sudarvizhi, K. Pandian, O.S. Oluwafemi, S.C.B. Gopinath, Amperometry detection of nitrite in food samples using tetrasulfonated copper phthalocyanine modified glassy carbon electrode, Sensors Actuators B Chem. 272 (2018) 151–159, https://doi.org/10.1016/j.snb.2018.05.147.

[36] J.M. Sousa, A.L. Ferreira, D.P. Fagg, E. Titus, R. Krishna, J. Gracio, Temperature dependence of the Henry's law constant for hydrogen storage in NaA zeolites: a Monte Carlo simulation study, J. Nanosci. Nanotechnol. 12 (2012) 6785–6791, https://doi.org/10.1166/jnn.2012.4569.

[37] N.P. Stadie, J.J. Vajo, R.W. Cumberland, A.A. Wilson, C.C. Ahn, B. Fultz, Zeolite-templated carbon materials for high-pressure hydrogen storage, Langmuir 28 (2012) 10057–10063, https://doi.org/10.1021/la302050m.

[38] D. Fairen-Jimenez, Y.J. Colon, O.K. Farha, Y.-S. Bae, J.T. Hupp, R.Q. Snurr, Understanding excess uptake maxima for hydrogen adsorption isotherms in frameworks with rht topology, Chem. Commun. 48 (2012) 10496–10498, https://doi.org/10.1039/c2cc35711a.

[39] Y.-H. Cheng, C.-Y. Zhang, J. Ren, K.-Y. Tong, Hydrogen storage in Li-doped fullerene-intercalated hexagonal boron nitrogen layers, Front. Phys. 11 (2016) 113101, https://doi.org/10.1007/s11467-016-0559-4.

[40] M. Doğan, P. Sabaz, Z. Bicil, B. Koçer Kızılduman, Y. Turhan, Activated carbon synthesis from tangerine peel and its use in hydrogen storage, J. Energy Inst. 93 (2020) 2176–2185, https://doi.org/10.1016/j.joei.2020.05.011.

[41] E. Poirier, A. Dailly, Investigation of the hydrogen state in IRMOF-1 from measurements and modeling of adsorption isotherms at high gas densities, J. Phys. Chem. C 112 (2008) 13047–13052, https://doi.org/10.1021/jp800981f.

[42] M. Thommes, K. Kaneko, A.V. Neimark, J.P. Olivier, F. Rodriguez-Reinoso, J. Rouquerol, K.S.W. Sing, Physisorption of gases, with special reference to the evaluation of surface area and pore size distribution (IUPAC technical report), Pure Appl. Chem. 87 (2015) 1051–1069, https://doi.org/10.1515/pac-2014-1117.

[43] G.A. El-Shobaky, M.A. Shouman, M.N. Alaya, Effects of Li_2O doping on the surface and catalytic properties of Co_3O_4–Fe_2O_3 solids precalcined at different temperatures, Adsorpt. Sci. Technol. 18 (2000) 239–252, https://doi.org/10.1260/0263617001493413.

[44] C.U. Deniz, H. Mert, C. Baykasoğlu, Li-doped fullerene pillared graphene nanocomposites for enhancing hydrogen storage: a computational study, Comput. Mater. Sci. 186 (2021) 110023, https://doi.org/10.1016/j.commatsci.2020.110023.

[45] J.H. Cho, C.R. Park, Hydrogen storage on Li-doped single-walled carbon nanotubes: computer simulation using the density functional theory, Catal. Today 120 (2007) 407–412, https://doi.org/10.1016/j.cattod.2006.09.027.

[46] D. Saha, S. Deng, Hydrogen adsorption on Pd- and Ru-doped C_{60} fullerene at an ambient temperature, Langmuir 27 (2011) 6780–6786, https://doi.org/10.1021/la200091s.

[47] D. Luxembourg, G. Flamant, E. Bêche, J.L. Sans, J. Giral, V. Goetz, Hydrogen storage capacity at high pressure of raw and purified single wall carbon nanotubes produced with a solar reactor, Int. J. Hydrog. Energy 32 (2007) 1016–1023, https://doi.org/10.1016/j.ijhydene.2006.07.005.

[48] A. Chamber, C. Park, R.T.K. Baker, N.M. Rodriguez, Hydrogen storage in graphite nanofibers, J. Phys. Chem. B 102 (1998) 4253–4256, https://doi.org/10.1021/jp980114l.

[49] M. Aghababaei, A.A. Ghoreyshi, K. Esfandiari, Optimizing the conditions of multi-walled carbon nanotubes surface activation and loading metal nanoparticles for enhanced hydrogen storage, Int. J. Hydrog. Energy 45 (2020) 23112–23121, https://doi.org/10.1016/j.ijhydene.2020.06.201.

[50] M. Doğan, A. Selek, O. Turhan, B.K. Kızılduman, Z. Bicil, Different functional groups functionalized hexagonal boron nitride (h-BN) nanoparticles and multi-walled carbon nanotubes (MWCNT) for hydrogen storage, Fuel 303 (2021) 121335, https://doi.org/10.1016/j.fuel.2021.121335.

[51] Ü. Çakır, F. Kestel, B. Koçer Kızılduman, Z. Bicil, M. Doğan, Multi walled carbon nanotubes functionalized by hydroxyl and Schiff base and their hydrogen storage properties, Diam. Relat. Mater. 120 (2021) 108604, https://doi.org/10.1016/j.diamond.2021.108604.

[52] Z. Bicil, M. Doğan, Characterization of activated carbons prepared from almond shells and their hydrogen storage properties, Energy Fuel 35 (2021) 10227–10240, https://doi.org/10.1021/acs.energyfuels.1c00795.
[54] Ö. Demirbaş, M. Alkan, M. Doğan, Y. Turhan, H. Namlı, P. Turan, Electrokinetic and adsorption properties of sepiolite modified by 3-aminopropyltriethoxysilane, J. Hazard. Mater. 149 (2007) 650–656, https://doi.org/10.1016/j.jhazmat.2007.04.036.
[55] M.I. Temkin, Adsorption equilibrium and the kinetics of processes on nonhomogeneous surfaces and in the interaction between adsorbed molecules, Zh. Fiz. Khim. 15 (1941) 296–332.
[56] F.O. Erdogan, Freundlich, Langmuir, Temkin and Harkins–Jura isotherms studies of H_2 adsorption on porous adsorbents, Chem. Chem. Technol. 13 (2019) 129–135, https://doi.org/10.23939/chcht13.02.129.
[57] S.V. Sawant, S. Banerjee, A.W. Patwardhan, J.B. Joshi, K. Dasgupta, Effect of in-situ boron doping on hydrogen adsorption properties of carbon nanotubes, Int. J. Hydrog. Energy 44 (2019) 18193–18204, https://doi.org/10.1016/j.ijhydene.2019.05.029.
[58] A. Nasruddin, M.I. Martin, D. Alhamid, Tampubolon, adsorption isotherms of hydrogen on granular activated carbon derived from coal and derived from coconut shell, Heat Transf. Eng. 38 (2017) 403–408, https://doi.org/10.1080/01457632.2016.1194703.
[59] D. Saha, Z. Wei, S. Deng, Hydrogen adsorption equilibrium and kinetics in metal–organic framework (MOF-5) synthesized with DEF approach, Sep. Purif. Technol. 64 (2009) 280–287, https://doi.org/10.1016/j.seppur.2008.10.022.
[60] H. Motaghi, P. Arabkhani, M. Parvinnia, A. Asfaram, Simultaneous adsorption of cobalt ions, azo dye, and imidacloprid pesticide on the magnetic chitosan/activated carbon@UiO-66 bio-nanocomposite: optimization, mechanisms, regeneration, and application, Sep. Purif. Technol. 284 (2022) 120258, https://doi.org/10.1016/j.seppur.2021.120258.
[61] M.H. Karaoğlu, M. Doğan, M. Alkan, Kinetic analysis of reactive blue 221 adsorption on kaolinite, Desalination 256 (2010) 154–165, https://doi.org/10.1016/j.desal.2010.01.021.
[62] M. Doğan, M. Alkan, Adsorption kinetics of methyl violet onto perlite, Chemosphere 50 (2003) 517–528, https://doi.org/10.1016/S0045-6535(02)00629-X.
[63] A. Dillon, K.M. Jones, T.A. Bekkedahl, C.H. Kiang, D.S. Bethune, M.J. Heben, Storage of hydrogen in single-walled carbon nanotubes, Nature 386 (1997) 377–379, https://doi.org/10.1038/386377a0.
[64] S. Kutluay, Benzen uçucu organik bileşiğinin badem kabuğundan üretilen char üzerine gaz fazı adsorpsiyonu: kinetik, denge ve termodinamik, Bitlis Eren Üniversitesi Fen Bilimleri Dergisi 8 (2019) 1432–1445, https://doi.org/10.17798/bitlisfen.543583.
[65] A.A. Haidry, Y. Jia, A. Raza, H. Zhu, A. Zavabeti, B. Saruhan, Elucidating the hydrogen adsorption kinetics on Pt/TiO_2/Pt based highly efficient sensors, Mater. Res. Bull. 167 (2023) 112415, https://doi.org/10.1016/j.materresbull.2023.112415.
[66] B. Bhangare, N.S. Ramgir, S. Jagtap, A.K. Debnath, K.P. Muthe, C. Terashima, D. K. Aswal, S.W. Gosavi, A. Fujishima, XPS and Kelvin probe studies of SnO_2/RGO nanohybrids based NO_2 sensors, Appl. Surf. Sci. 487 (2019) 918–929, https://doi.org/10.1016/j.apsusc.2019.05.176.
[67] M. Doğan, Y. Turhan, B.K. Kızılduman, P. Turan Beyli, S. Doğan, Isothermal calcination kinetics of boric acid and its use for nano boron oxide production under cryogenic conditions, Inorg. Nano-Met. Chem. (2024) 1–10, https://doi.org/10.1080/24701556.2024.2356039.
[68] M. Doğan, M. Alkan, Ö. Demirbaş, Y. Özdemir, C. Özmetin, Adsorption kinetics of maxilon blue GRL onto sepiolite from aqueous solutions, Chem. Eng. J. 124 (2006) 89–101, https://doi.org/10.1016/j.cej.2006.08.016.
[69] M. Alkan, M. Doğan, Y. Turhan, Ö. Demirbaş, P. Turan, Adsorption kinetics and mechanism of maxilon blue 5G dye on sepiolite from aqueous solutions, Chem. Eng. J. 139 (2008) 213–223, https://doi.org/10.1016/j.cej.2007.07.080.
[70] K.O. Yoro, M.K. Amosa, P.T. Sekoai, J. Mulopo, M.O. Daramola, Diffusion mechanism and effect of mass transfer limitation during the adsorption of CO_2 by polyaspartamide in a packed-bed unit, Int. J. Sustain. Eng. 13 (2020) 54–67, https://doi.org/10.1080/19397038.2019.1592261.
[71] C. Nareswari, U. Zulfiani, A. Junaidi, T. Gunawan, N. Widiastuti, Adsorption of CO_2 and H_2 on the polymer-based membrane from high-density polyethylene (HDPE) plastic, S. Afr. J. Chem. Eng. 49 (2024) 105–113, https://doi.org/10.1016/j.sajce.2024.04.004.
[72] M.S.M. Zaini, M. Arshad, S.S.A. Syed-Hassan, Adsorption isotherm and kinetic study of methane on palm kernel shell-derived activated carbon, J. Bioresour. Bioprod. 8 (2023) 66–77, https://doi.org/10.1016/j.jobab.2022.11.002.